RSC Advances

PAPER

View Article Online
View Journal | View Issue

Cite this: *RSC Adv.*, 2026, **16**, 8921

Dual-targeting sulfamethoxazole derivatives overcome multidrug resistance in ESKAPE pathogens by inhibiting quorum sensing and efflux pumps

Benedicta Yayra Adzah,[a] Prince Danan Biniyam,[a] Victoria Ohene-Adu,[a] Michael Osei,[a] Kwabena Adu-Adjei,[a] Victoria Elmes,[b] Iain Goodall,[b] Vuvor Faustina,[a] Yvonne Dogbeda Agboyibor,[a] Patrick Gyan,[a] Paul Quansah,[a] Cyril Makafui Amengor,[c] Joshua Boateng,[b] En Zhang,[d] Maxwell Ampomah-Wireko,[d] Ernest Oyeh[e] and Cedric Dzidzor Kodjo Amengor *[a]

The rapid emergence of pan-drug-resistant pathogens necessitates innovative antimicrobial strategies that overcome conventional resistance. This study reports the structure-guided design of sulfamethoxazole derivatives as dual inhibitors of quorum sensing (LasR) and efflux pumps (AcrB), alongside the classic dihydropteroate synthase (DHPS) target. High-throughput virtual screening of 54 derivatives, followed by MM-GBSA analysis, prioritized five novel compounds for synthesis. Their structures were confirmed by $^{1}H/^{13}C$ NMR, FT-IR, and mass spectrometry. All compounds demonstrated potent growth inhibition (MICs 15.625–125 μg mL^{-1}) against *Proteus mirabilis*, *Salmonella typhi*, and *Escherichia coli*, though activity against the more resistant *Pseudomonas aeruginosa* was reduced. Critically, lead compounds **SMX033** and **SMX015** achieved >99% biofilm inhibition against *P. mirabilis*, and **SMX033** showed significant efflux pump inhibition, directly validating our *in silico* predictions of a multi-target mechanism. In particular, compound **SMX033** exhibited the best antimicrobial activity and lowest cytotoxicity of all the sulfamethoxazole derivatives with a CCC_{50} value of 286.20 μM against *Vero cells*. Despite their predicted *in silico* genotoxicity, these derivatives provide promising chemical scaffolds for combating multidrug-resistant infections by concurrently attenuating virulence and restoring antibiotic susceptibility.

Received 19th October 2025
Accepted 26th January 2026

DOI: 10.1039/d5ra08024j

rsc.li/rsc-advances

1 Introduction

Bacterial-related infectious diseases pose a significant threat to global health due to their clinical diversity, high transmissibility, and the rapid emergence of antibiotic-resistant strains.[1] These infections are the leading causes of morbidity and mortality worldwide.[2] Antimicrobial resistance is a pressing global concern, as microorganisms develop resistance to existing antibiotics, rendering many treatments ineffective.[3,4] This highlights the urgent need for novel antimicrobial agents with broad-spectrum efficacy, particularly against multidrug-resistant strains.

Heterocyclic compounds have become a cornerstone in medicinal chemistry because of their potential versatile pharmacological activities.[3] Therefore, synthetic medicinal chemists usually introduce a heterocyclic moiety, representing 85%, in the design of most drugs in order to enhance pharmacological activity while addressing metabolism and pharmacokinetic issues.[3,4] Despite their ease of synthesis, the heterocyclic core imparts the clinical drug candidate with suitable pharmacokinetic properties.[4] Most drugs fail to move from the bench to the patient because of poor pharmacokinetic profiles; therefore, the introduction of the heterocyclic groups can contribute to reducing the attrition rate of promising clinical candidates while improving the efficacy and toxicity profiles.[5]

The isoxazole class of heterocyclics continues to make an immense contribution to the drug discovery pipeline with the introduction of drugs possessing anti-inflammatory, antimicrobial, antioxidant, and other anti-infective properties.[6,7] Drugs that possess the isoxazole group include sulfamethoxazole, sulfisoxazole, flucloxacillin, valdecoxib, leflunomide, and isoxicam[8,9] (Fig. 1). One of the most common and clinically useful sulphonamides, sulfamethoxazole, is an antimicrobial

[a]*Department of Pharmaceutical Chemistry, Drug Discovery Unit, School of Pharmacy, University of Health and Allied Sciences, Ho, Ghana. E-mail: camengor@uhas.edu.gh; Tel: +233246456764*

[b]*School of Science, University of Greenwich, UK*

[c]*Department of Mathematics, University of Ghana, Legon, Ghana*

[d]*School of Pharmaceutical Sciences, Key Laboratory of Advanced Pharmaceutical Technology, Ministry of Education of China, Zhengzhou University, Zhengzhou 450001, PR China*

[e]*Department of Nursing, Faculty of Science, Methodist University Ghana, Ghana*

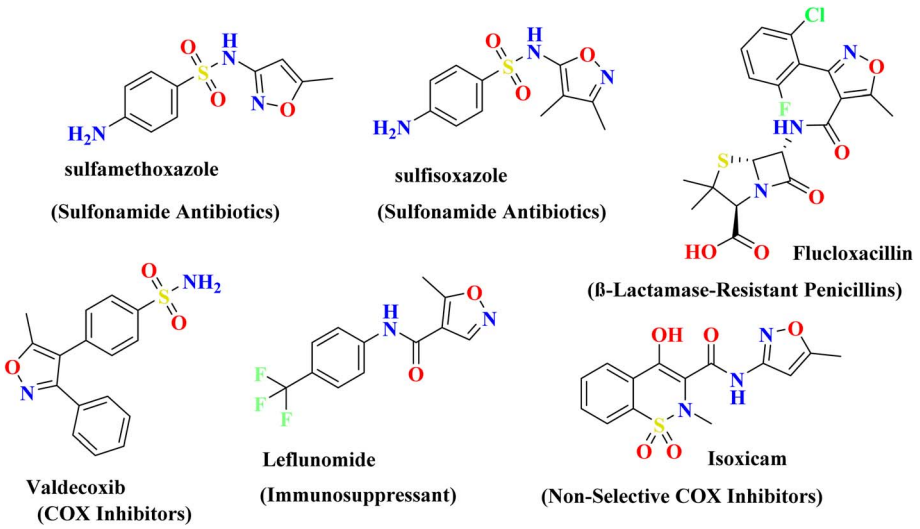

Fig. 1 Some isoxazole containing biological active heterocyclic compounds.

drug used in combination with trimethoprim for the treatment of bacteria-related infections.[10,11] It has established activity against Gram-positive and Gram-negative organisms, rendering it a broad-spectrum antibiotic, but it is gradually losing potency due to antimicrobial resistance.[12] Current studies have demonstrated that sulfamethoxazole derivatives possess antimicrobial properties, and they represent promising clinical candidates. These include sulfamethoxazole ligand metal complexes, which showed potency against some ESKAPE pathogens (*Staphylococcus aureus*, *Escherichia coli*, and *Klebsiella pneumoniae*) and fungal strains of Aspergillus, and these complexes have the ability to inhibit bacterial biofilm formation.[13,14] They have also been shown to inhibit the growth of virulent forms of *Mycobacteria* by blocking biofilm formation and efflux pumps of the bacteria.

Sulfonamides inhibit the *para*-amino benzoic acid (PABA) pathway, blocking folate synthesis required for DNA replication. However, the approach of drug discovery through targeting this bacteria mechanism is no longer effective due to antibiotic resistance.[15,16] Moreover, the development of multi-drug resistance to sulfamethoxazole has also been attributed to mutation and generation of new resistance genes, quorum sensing, biofilm formation, presence of efflux pumps, and redundancy of the known inhibitory pathways.[17–19] This has rendered the drug sulfamethoxazole/trimethoprim (co-trimoxazole) ineffective as the first choice of drug for the treatment of most infections.

The application of computational methods such as molecular docking and molecular dynamics simulations has greatly enhanced our understanding of how sulfamethoxazole derivatives interact with biological targets such as DHPS.[20] These approaches provide high-resolution information about binding affinities, conformational dynamics, and molecular recognition.[21] This combination of computational and experimental approaches has become an important part of current drug development, allowing for the rapid identification and optimization of new sulfamethoxazole compounds with enhanced pharmacological characteristics.[22–24]

In this current study, we employed a computationally guided approach to design a library of sulfamethoxazole derivatives targeting DHPS, LasR, and AcrB, and to explore their resulting potential new phenotypic antibacterial, efflux pump inhibitory, and biofilm inhibitory activities.

2 Experimental design

The study involved 54 sulfamethoxazole derivatives, with sulfamethoxazole as a benchmark drug.[25] Ligands were designed using positional isomerization of 19 diverse substituents, electron donating (dimethylamino, hydroxy, methoxy, ethoxy, methylthio, methyl, acetamido), electron withdrawing (nitro, cyano, trifluoromethyl, carboxylic acid, methyl ester, sulfonic acid, formyl), and halogens (bromo, chloro, fluoro), on the aromatic ring of the sulfamethoxazole (SMX) core. Molecular docking and MMGBSA calculations were performed on DHPS, LasR, and AcrB proteins to estimate binding free energy. Five sulfamethoxazole derivatives were prioritized for synthesis from the *in silico* screening and antimicrobial evaluation, focusing on synthetic accessibility, structural diversity, and resource efficiency.

3 Chemistry

The chemicals used for the synthesis were purchased from Merck® (Gillingham, UK) and were of analytical grade, except for the HPLC-grade solvents (methanol and acetonitrile) sourced from Fischer Scientific (Loughborough, UK). The progress of the reaction and the purity of the synthesized compounds were monitored by thin-layer chromatography (TLC) using aluminum plates pre-coated with silica gel, observed at a fluorescence wavelength of 254 nm. A calibrated pH meter (Eutech Instruments ECPH70042GS, Singapore) was employed to monitor the pH, which in turn offered information about the progress of the reaction. The purity of the compounds was further assessed by determining their melting points using

a B-540 analyzer for melting points (Büchi Corporation, New Castle, DE, USA), and the reported melting points are uncorrected. The presence of key functional groups in the synthesized compounds was recorded using a PerkinElmer Spectrum 100 FT-IR spectrometer (PerkinElmer Inc., Waltham, MA, USA) equipped with attenuated total reflectance mode. NMR spectra were acquired on a Bruker Ascend III (500 MHz) spectrometer (Bruker BioSpin AG, Fällanden, Switzerland). Chemical shifts were reported in parts per million (δ) relative to tetramethylsilane (TMS), with the residual solvent serving as the lock solvent ([D6] DMSO, $\delta = 2.50$ ppm for 1H and $\delta = 39.52$, 77.5 ppm for 13C). High-resolution mass spectra were obtained using an HPLC (Shimadzu LC-2010A) in conjunction with a time-of-flight (quadrupole mass analyzer) mass spectrometer operating in positive ESI ionization mode.

3.1 General procedure for the synthesis of the sulfamethoxazole hybrids[25]

A mixture of 3-amino-5-methylisoxazole (2.5 mmol, 1 equiv.) and substituted sulfonyl chlorides (2.5 mmol, 1.0 equiv.) was suspended in 30 mL of water. The pH of the suspension was adjusted and maintained at 8.0 by adding a 1 M Na_2CO_3 aqueous solution at room temperature and monitored using a pH meter probe. The progress of the reaction was tracked using TLC with a developing solvent of (CH_2Cl_2) : (Et_2O) [60 : 40]. Upon completion of the reaction, concentrated HCl was added slowly to lower the pH to 2.0. The resulting precipitate was collected by suction filtration, washed with water, and dried to yield the crude compound. The crude product was purified by silica column chromatography using a dichloromethane (CH_2Cl_2) : diethyl ether (Et_2O) [60 : 40] mobile phase through gradient elution to isolate the target compounds as solid products.

3.2 Spectral data

3.2.1 *N*-(5-Methylisoxazol-3-yl)-2-nitrobenzenesulfonamide (SMX001). White solid. Yield (0.482 g, 52%), m.p. 116–118 °C; R_f: 0.75, FT-IR (ν/cm): 2952, 2831, (aliphatic –CH), 1649 (–C=O), 1566 (–C=C**H**–), 822, 798, 524 (Ar–C–H), ^{1}H NMR (400 MHz, $CDCl_3$ δ ppm), 8.12 (2H, m, –ArH), 7.86 (1H, m, –ArH), 7.75 (1H, m, –ArH), 6.17 (1H, q, –ArN**H**$_{isox}$), 2.95 (br, 1H, s, –$NHSO_2$–), 2.36 (3H, d, $J = 4.00$ Hz –$ArCH_3$); ^{13}C NMR (400 MHz, $CDCl_3$ δ ppm) δ; 171.04, 156.97, 134.44, 132.79, 132.60, 131.45, 125.38, 96.02, 12.67; HRMS (ESI): m/z calculated for $C_{10}H_9N_3O_5S$: 283.0263, found, $[M + H]^+$: 284.0327.

3.2.2 *N*-(5-Methylisoxazol-3-yl)-4-nitrobenzenesulfonamide (SMX003). Beige solid. Yield (0.482 g, 68%), m.p. 118–120 °C; R_f: 0.75, FT-IR (ν/cm): 2952, 2831, (aliphatic –CH), 1649 (–C=O), 1566 (–C=C**H**–), 822, 798, 524 (Ar–C–H), ^{1}H NMR (400 MHz, $CDCl_3$ δ ppm), 8.34 (2H, d. $J = 8.00$, –ArH), 8.08 (2H, d, $J = 8.00$, –ArH), 7.13 (1H, m, –ArH), 6.18–6.17 (1H, q, –ArN**H**$_{isox}$), 2.56 (br, 1H, s, –$NHSO_2$–), 2.36–2.35 (3H, d, $J = 4.00$ Hz –$ArCH_3$); ^{13}C NMR (400 MHz, $CDCl_3$ δ ppm) δ; 171.17, 157.20, 145.12, 128.49, 124.47, 95.56, 50.20, 48.92, 49.78, 29.73, 12.67; HRMS (ESI): m/z calculated for $C_{10}H_9N_3O_5S$: 283.0263, found, $[M + H]^+$: 284.0329.

3.2.3 Methyl 4-(*N*-(5-methylisoxazol-3-yl) sulfamoyl) benzoate (SMX015). Beige solid. Yield (0.5493 g, 75%), m. p. 126–129 °C; R_f: 0.65, FT-IR (ν/cm): 2952, 2831, (aliphatic –CH), 1649 (–C=O), 1566 (–C=C**H**–), 822, 798, 524 (Ar–C–H), ^{1}H NMR (400 MHz, $CDCl_3$ δ ppm) 8.48 (br, 1H, s, –$NHSO_2$–), 8.15 (2H, d, $J = 8.00$ Hz, –ArH), 7.91 (2H, d, $J = 8.00$ Hz, –ArH), 6.26–6.24 (1H, q, –ArN**H**$_{isox}$), 3.95 (3H, s, –OCOC**H**$_3$), 2.31 (3H, s, –$ArCH_3$) ^{13}C NMR (400 MHz, $CDCl_3$ δ ppm) δ; δ; 171.38, 165.37, 142.67 134.64, 130.49, 127.13, 95.55, 52.74, 21.60, 12.73; HRMS (ESI): m/z calculated for $C_{12}H_{12}N_2O_5S$: 296.0567, found, $[M + H]^+$: 297.0535.

3.2.4 2-Bromo-*N*-(5-methylisoxazol-3-yl) benzenesulfonamide (SMX019). Pale brown solid. Yield (0.550 g, 71%), m.p. 164–167 °C; R_f: 0.66, FT-IR (ν/cm): 2952, 2831, (aliphatic –CH), 1649 (–C=O), 1566 (–C=C**H**–), 822, 798, 524 (Ar–C–H), ^{1}H NMR (400 MHz, $CDCl_3$ δ ppm) 8.56 (br, 1H, s, –$NHSO_2$–), 8.13 (1H, m, –ArH), 7.45 (1H, m, –ArH), 7.13–7.18 (2H, d, $J = 8.00$ Hz, –ArH), 6.11–6.10 (1H, q, –ArH$_{isox}$), 2.31 (3H, s, –$ArCH_3$) ; ^{13}C NMR (400 MHz, $CDCl_3$ δ ppm) δ; 171.01, 156.67, 138.03, 135.50, 134.56, 131.56, 127.79, 120.20, 95.27, 12.68; HRMS (ESI): m/z calculated for $C_{10}H_9{}^{35}B_rN_2O_3S$: 315.9517, found, $[M + H]^+$: 316.9591; calculated for $C_{10}H_9{}^{37}B_rN_2O_3S$: 316.9517, found, $[M + 2]^+$: 318.9565.

3.2.5 4-Methyl-*N*-(5-methylisoxazol-3-yl) benzenesulfonamide (SMX033). Beige solid. Yield (0.4110 g, 65%), m.p. 125–127 °C; R_f: 0.52, FT-IR (ν/cm): 2952, 2831, (aliphatic –CH), 1649 (–C=O), 1566 (–C=C**H**–), 822, 798, 524 (Ar–C–H), ^{1}H NMR (400 MHz, $CDCl_3$ δ ppm) 8.24 (br, 1H, s, –$NHSO_2$–), 7.74–7.72 (2H, d, $J = 8.00$ Hz, –ArH), 7.70–7.68 (1H, d, $J = 8.00$ Hz, –ArH), 6.26–6.24 (1H, q, –ArN**H**$_{isox}$), 2.40 (3H, s, –$ArCH_3$), 2.37–2.36 (3H, d, $J = 4.00$ m –$ArCH_3$) ^{13}C NMR (400 MHz, $CDCl_3$ δ ppm) δ 171.01, 157.53, 144.56, 136.02, 129.92, 127.10, 95.55, 21.60, 12.73; HRMS (ESI): m/z calculated for $C_{11}H_{12}N_2O_3S$: 252.0569, found, $[M + H]^+$:253.0649.

4 Antimicrobial assay

4.1 Minimum inhibitory concentration assay

To determine the minimum inhibitory concentration (MIC), the micro-well dilution method outlined by Fetse *et al.* (2014) and Agyare *et al.* (2013) was used.[26,27] This approach measures the development/growth of microorganisms at different antimicrobial concentrations. Aqueous solutions of the compounds were prepared at a concentration of 200 mg mL^{-1} by dissolving 0.6 g of each synthesized compound in 3 mL of sterile water. In 96-well plates, 100 µL of double-strength broth was added to each well, followed by the addition of the compounds at a series of doubling dilutions, with final concentrations ranging from 250 to 3.91 µg mL^{-1}. The test organisms, standardized to an inoculum size of 1×10^6 CFU mL^{-1} using the 0.5 M MacFarland standard, were then added to each well at a volume of 20 µL. The plates were covered and incubated at 37 °C for 24 hours. After the incubation period, 25 µL of 1.25 mg mL^{-1} of 3-(4,5-dimethylthiazol-2-yl)-2,5-diphenyltetrazolium bromide (MTT) solution was added to each well and further incubated at 37 °C for 30 minutes. The MIC was determined as the lowest concentration at which no visible change in colour from yellow

to purple occurred following the addition of MTT, indicating no microbial growth.

4.2 Crystal violet biofilm inhibition assay

The biofilm inhibitory activity against *Proteus mirabilis*, *Salmonella typhi*, *Escherichia coli*, and *Pseudomonas aeruginosa* was evaluated using a modified assay that retains crystal violet, adapted from Ofori *et al.* (2021).[28] Bacterial cultures were grown on brain heart infusion (BHI) agar at 37 °C for 24 hours. Colonies were suspended in BHI broth and adjusted to 0.5 McFarland standard ($\sim 1.5 \times 10^8$ CFU mL^{-1}) using sterile saline. In sterile 96-well plates, 100 μL of standardized bacterial suspension was combined with 100 μL of BHI broth containing test compounds at final sub-MIC concentrations. Wells containing bacteria without compounds served as growth controls, while wells with BHI broth alone served as blanks. Plates were wrapped in aluminum foil and incubated statically at 37 °C for 24 hours. After incubation, planktonic cells were aspirated, and wells were washed three times with 200 μL phosphate-buffered saline (PBS, pH 7.4) to remove non-adherent cells. Adherent biofilms were fixed with 150 μL methanol for 15 minutes, stained with 0.1% (w/v) crystal violet for 15 minutes, and washed three times with distilled water. Bound dye was solubilized with 150 μL of 95% ethanol for 30 minutes. Absorbance was measured at 630 nm using a microplate reader (BioTek Synergy H1, USA). Percentage biofilm inhibition was calculated as:

$$\text{Inhibition}(\%) = 1 - \frac{\text{OD test} - \text{OD blank}}{\text{OD growthcontrol} - \text{OD blank}} \times 100$$

Each compound-pathogen combination was tested in triplicate wells across three independent experiments.

4.3 Ethidium bromide efflux pump inhibition assay

Efflux pump inhibition was assessed against *P. mirabilis*, *S. typhi*, *E. coli*, and *P. aeruginosa* using an ethidium bromide accumulation assay as reported by Danquah *et al.* (2018).[29] Bacteria were cultured in nutrient broth with 0.4% glucose at 37 °C (150 rpm) until OD_{600} reached 0.8–1.0. Cells were centrifuged (3000×*g*, 10 min), washed twice with PBS, and resuspended in PBS to $OD_{600} = 0.4$. Aliquots (250 μL) of bacterial suspension were transferred into Eppendorf tubes containing sub-MIC concentrations ($\frac{1}{2}$ MIC) of test compounds. Controls included: positive control: 250 μL bacteria + 20 μg mL^{-1} verapamil. Negative control: 250 μL bacteria (no inhibitor). Blank: 250 μL PBS. Glucose (1.5 μL of 80% w/v) was added to energize efflux pumps. After pre-incubation (37 °C, 10 min), 2.5 μL EtBr (50 mg L^{-1}) was added. Immediately, 250 μL aliquots were transferred to black 96-well plates. Fluorescence ($\lambda_{ex} = 530$ nm, $\lambda_{em} = 600$ nm) was measured every minute for 60 min at 37 °C (BioTek Synergy H1). Relative fluorescence was plotted against time, and efflux pump inhibition was quantified by calculating the area under the curve (AUC) for fluorescence kinetics.[30] All assays were performed in triplicate with three biological replicates.

4.4 *In vitro* cytotoxicity

The *in vitro* cytotoxicity of the synthesized compounds were assessed using Vero cells (kidney cells from African green monkey: ATCC CCL-81) following the standard MTT method.[30] The average absorbances of triplicate cells were recorded and used to determine the % growth inhibition was determined using the formula: 100 − [sample absorbance/control absorbance] × 100.

5 Computational methods

5.1 Protein selection and preparation

Bacterial drug targets related to bacterial folic acid biosynthesis (3TZF), bacterial multidrug exporters (2W1B), and biofilm formation (6V7X) were considered in the molecular docking studies. Inhibiting folic acid biosynthesis eventually disrupts bacterial DNA replication, stability, and integrity, while targeting multidrug exporters and biofilm-related pathways reduces bacterial resistance and enhances treatment efficacy.[31] The 3D structure of protein targets complexed with native ligands was retrieved from the Protein Data Bank (https://www.rcsb.org/). The protein structures were imported and pre-processed in Discovery Studio 2025 Client by deleting heteroatoms. Protein structures containing multiple identical chains were examined, and, for cases where the chains were structurally equivalent and each contained the active site, only one chain was retained to eliminate redundancy and minimize computational complexity. The protein structures were energy minimized using the AMBERf4SB force field, with Gasteiger charges assigned using Antechamber in Chimera to enhance the models for molecular docking and MMGBSA calculations.[32]

5.2 Ligand preparation and ADME-TOX

The 2D and 3D molecular structures of sulfamethoxazole and a curated library of 54 sulfamethoxazole derivatives were modeled and geometry-optimized using Avogadro molecular modeling software. Energy minimization was performed using the General Amber Force Field (GAFF) to refine the chemical structures and ensure accurate molecular geometries and electronic properties.[33] Partial atomic charges were assigned *via* the Gasteiger method, and polar hydrogens were incorporated using UCSF Chimera. The final structures were exported in Sybyl Molecular Model (MOL2) and Structure Data File (SDF) formats for subsequent computational analyses, including molecular docking simulations and scoring assessments.

Pharmacokinetic properties, such as absorption, distribution, metabolism, and excretion of the designed sulfamethoxazole derivative, were predicted from ADMETLAB 3.0 and SwissADME web servers. Toxicity parameters were assessed *via* Data Warrior software and ADMETLAB 3.0.

5.3 Molecular docking

Molecular docking was employed to explore the binding mechanisms of the sulfamethoxazole derivatives. A blind docking approach utilizing AutoDock Vina software was employed to generate the optimal binding poses and

interactions between the modeled ligands and the prepared DHPS, AcrB, and LasR proteins.[34] In this method the grid box was programmed to encompass the entire protein structure (bind docking) without predefining any residues as critical for binding. This approach ensures that the ligand has the opportunity to interact with any portion of the protein, allowing the identification of potential binding pockets and enabling the ligand to bind to the most favorable site. The molecular docking protocol was validated by retrieving the 3D structure of the native ligand co-crystallized with *P. aeruginosa* LasR protein from the Protein Data Bank. The ligand was redocked onto the protein structure using AutoDock Vina and a blind docking approach. Five exhaustiveness values (8, 64, 128, 512, and 1064) were tested to evaluate the influence of sampling thoroughness on the redocking accuracy.[35] An improvement in accuracy was observed when increasing exhaustiveness from 8 to 64, while higher values provided no substantial additional benefit. An exhaustiveness value of 64 was selected for all subsequent docking runs. Root mean square deviation and interaction maps were assessed to ensure the accuracy of the docking protocol. The consistency of key interactions between the redocked ligand and the protein was also checked in relation to the experimentally determined binding site. This multi-faceted validation approach ensures the reliability, reproducibility, and accuracy of the docking protocol.

5.4 Ligand efficiency

Ligand efficiency is a metric for evaluating the binding efficiencies of a ligand relative to its size. Ligand efficiency was calculated using the following formula:

$$\text{Ligand efficiency} = \frac{\Delta G}{\text{HAC}}$$

where ΔG is the binding free energy (in kcal mol^{-1}), HAC represents heavy atom count, which is the number of non-hydrogen atoms in the ligand.

5.5 MM-PBSA calculations

The Molecular Mechanics Generalized Born Surface Area (MM-GBSA) method was used to estimate the binding free energy ($\Delta G_{binding}$) between the protein and the optimized docked poses of each ligand. Binding free energies were calculated as the difference in free energy between the ligand–protein complex and the unbound states of the protein and ligand.[36] The binding free energy was computed according to the following relationship:

$$\Delta G_{binding} = \Delta G_{complex} - \Delta G_{ptotein} - \Delta G_{ligand}$$

$\Delta G_{binding}$ is further decomposed into gas-phase interaction energy (ΔG_{gas}) and solvation free energy (ΔG_{solv}). This approach enabled a robust comparison of ligand affinities and facilitated the selection of promising candidates for further analysis.

5.6 Molecular dynamics simulations

SMX015 and **SMX033**, selected based on docking performance and experimental validation, were subjected to molecular dynamics (MD) simulations in complex with DHPS and LasR, together with their respective apo forms. Simulations were performed using GROMACS 2023,[37] with system preparation carried out using the CHARMM-GUI Solution Builder.[38] Systems were solvated in TIP3P water boxes extending 10 Å from the protein surface and neutralized with 0.15 M NaCl.[39] Protein parameters were assigned using the CHARMM36m force field, and ligand parameters were generated with CGenFF.[40] Following energy minimization (10 000 steps, steepest descent), systems were equilibrated under NVT (2 ns, 303.15 K, v-rescale thermostat) and NPT (5 ns, 1 bar, C-rescale barostat) conditions. Production simulations were conducted for 100 ns using a leapfrog integrator (2 fs timestep). Hydrogen bonds were constrained with LINCS, long-range electrostatics were treated using PME (1.2 nm cutoff), and van der Waals interactions were smoothly switched between 1.0 and 1.2 nm.

Trajectory analyses were performed using GROMACS 2023.1. Structural stability and dynamics were evaluated using RMSD, RMSF, radius of gyration (R_g), and solvent-accessible surface area (SASA). Principal component analysis (PCA) was used to identify dominant conformational motions, and non-bonded interaction energies were computed to characterize ligand-binding energetics.

6 Results and discussion

6.1 Integrated computational profiling

6.1.1 ADME-TOX. A computational approach was used to prioritize compounds for synthesis, combining pharmacokinetic profiling with binding pose validation and free energy calculations. The initial assessment of 54 sulfamethoxazole derivatives revealed structure–property relationships about their pharmacokinetic profile (Tables 1 and 2).

Predicted properties were classified using an empirical decision scale: values between 0.0–0.3 were considered

Table 1 Physicochemical, solubility and ADME properties of some of the prioritized sulfamethoxazole derivatives

Compound ID	MW (Da)	TPSA (Å^2)	log *S*	GI absorption	PPB	BBB permeant
SMX033	252.06	72.2	−3.3378	High	92.00938	No
SMX015	296.05	98.5	−2.90194	High	92.75873	No
SMX019	315.95	72.2	−3.49824	High	94.69174	No
SMX003	283.03	115.34	−3.07732	High	85.5729	No
SMX001	283.03	115.34	−3.22374	High	95.448	No
SMX	253.05	98.22	−2.64664	High	61.27968	No

Table 2 Continuation of physicochemical, solubility and ADME properties of some of the prioritized sulfamethoxazole derivatives

Compound ID	hERG	DILI	BSEP	Nephrotoxicity-DI	Neurotoxicity-DI
SMX033	0.075765	0.999 766	0.987 738	0.113 391	0.034758
SMX015	0.043284	0.999 995	0.916 285	0.043675	0.012197
SMX019	0.042108	0.999 762	0.998 342	0.068108	0.042637
SMX003	0.061045	0.999 999	0.749 857	0.068014	0.001445
SMX001	0.035825	0.999 983	0.809 684	0.069278	0.006155
SMX	0.036709	0.999 988	0.004074	0.071402	0.102 531

excellent, 0.3–0.7 moderate, and 0.7–1.0 poor facilitating rapid prioritization of compounds.

The derivatives were found to have favourable oral absorption potential, but aqueous solubility was a major limitation, particularly for those featuring strong electron-withdrawing groups. This property could be improved by perhydrating the isoxazole ring of the potential drug-like derivatives.[40] Positional isomerism also influenced distribution and metabolic stability. *para*-Substituted derivatives consistently demonstrated enhanced intestinal permeability relative to *ortho* or *meta* isomers.[41] This geometric dependence extends to plasma protein binding, where *ortho*-substituted derivatives exhibit elevated affinity due to restricted conformational freedom promoting hydrophobic interactions.[42] Metabolic susceptibility follows distinct electron gradients, with electron-donating groups reducing CYP450 inhibition liabilities and nitro and cyano substituents elevating risk for CYP3A4 and CYP2C19.[43] Toxicity profiling revealed organ-specific risk stratification. Hepatotoxicity (DILI) correlated strongly with BSEP inhibition, which is linked to bile acid accumulation and mitochondrial dysfunction.[44] Cardiotoxicity risks diverged significantly, with **SMX052** showing a high predicted risk of severe hERG inhibition, which is potentially fatal. Neurotoxicity and nephrotoxicity probability depend on transport inhibition profiles, underscoring the necessity of integrated assessment of off-target effects at hepatic or renal transporters. Compound **SMX012** (*para*-carboxylic acid) showed favourable solubility, negligible hERG inhibition, less BBB permeability, and low DILI risk, positioning it as a candidate for consideration. Trifluoromethyl derivatives were removed due to high PPB and BSEP inhibition. Furthermore, **SMX016** (hepatotoxic) and **SMX052** (cardiotoxic) were excluded due to intractable safety liabilities, while moderate-risk candidates such as **SMX042** may require medicinal chemistry refinement to reduce CYP2C9 inhibition.

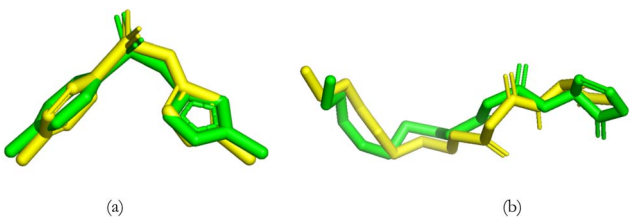

Fig. 2 Validation of the molecular docking protocol. (a) Superposition of the co-crystallized ligand O8D (green) with its redocked pose (yellow), yielding a root-mean-square deviation (RMSD) of 0.03 Å, indicating accurate reproduction of the experimental conformation. (b) Superposition of the co-crystallized ligand OHN (green) with its redocked pose (yellow), with an RMSD of 0.20 Å, confirming the reliability of the docking procedure.

6.1.2 Molecular docking and ligand efficiency matrix. Molecular docking calculations were employed to identify potential DHPS inhibitors from the ADME-TOX filtered designed compounds. This docking experiment was conducted prior to investigating the effective derivatives on the LasR and AcrB protein targets. The method indicates a promising pathway for the development of new sulphonamide agents with dual mechanisms of action against bacterial cells.

The molecular docking protocol was initially validated by redocking the bound ligand *N*-3-oxo-dodecanosyl-homoserine lactone (OHN) and sulphonamide drug (08D) with LasR and DHPS, respectively, using Autodock Vina software (Fig. 2 &3). As expected, redocked ligands tended to have lower calculated energy values. A root mean square deviation (RMSD) of 0.20 Å was obtained for the highest OHN-ranked pose, while a value of 1.12 Å was recorded for the lowest-ranked OHN pose. The RMSD values of the sulphonamide drug (O8D) were between 0.03 and 0.67 Å. These low RMSD values (RMSD < 2 Å) suggest that the docking protocol and scoring function employed can accurately reproduce the native binding pose.[45] Furthermore, the redocked poses of the top-ranked eight complexes maintained all key interactions, implying that they were oriented in a biologically relevant manner within the binding sites, making the redocking parameters suitable for docking the designed compounds against the protein targets.[46]

The docking scores of the designed compounds ranged from −4.13 to −6.78 kcal mol^{-1}, with the benchmark drug, sulfamethoxazole, exhibiting a score of −4.79 kcal mol^{-1}. The results revealed a spectrum of binding affinities among the compounds, indicating potential for further investigation. The compounds were divided into four clusters based on docking score (*D*-score) and ligand efficiency, with more negative *D*-scores indicating stronger predicted binding affinities (Fig. 4). Electron-withdrawing (EWG) substituents consistently showed stronger binding affinities than electron-donating counterparts, as the sulfonamide group served as a hydrogen bond acceptor. The most potent derivative, **SMX-018**, possesses a *para*-sulfonic acid moiety, a strong EWG, achieving a docking score of −6.78 kcal mol^{-1}. Analogues with other strong EWGs, such as carboxylic acids and trifluoromethyl groups, show moderate docking scores. Compounds functionalized with electron-donating groups exhibit moderate binding, with their docking scores clustering in a less negative range.[47] The least potent

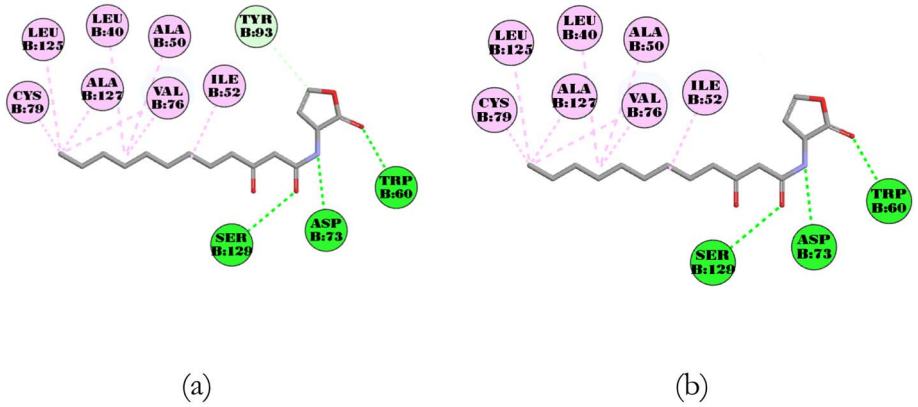

Fig. 3 (a) Two-dimensional interaction diagram of the co-crystallized ligand OHN in complex with 6V7X before redocking. (b) A two-dimensional interaction diagram of the same ligand after redocking, demonstrating the retention of key binding interactions within the active site.

compounds are those substituted with strong *para*-directed EDGs, such as *p*-dimethylamino, *p*-ethoxy, and *p*-nitro. The ligand efficiency (L.E.) metric generally trends with the *D*-score, confirming that the improved binding of EWG analogues is not an artifact of increased molecular size but a more efficient interaction.[48]

Sulfamethoxazole inhibits DHPS through conserved interactions, including the electrostatic anchoring of its sulfonyl group to Lys^{221} and π-stacking of its aniline ring with Phe^{190}.[49] To address the limitations related to resistance, our structure-guided optimization procedure yielded sulfamethoxazole derivatives that created a comprehensive interaction network with the DHPS active site, as shown in Fig. 5a–d. Protein-ligand analysis identified hydrogen bonds with residues Arg^{235}, Ser^{222}, Thr^{62}, Pro^{64}, Gly189, and Lys^{221}, as well as extended hydrophobic interactions through π-stacking with Phe^{28} and Phe^{190},

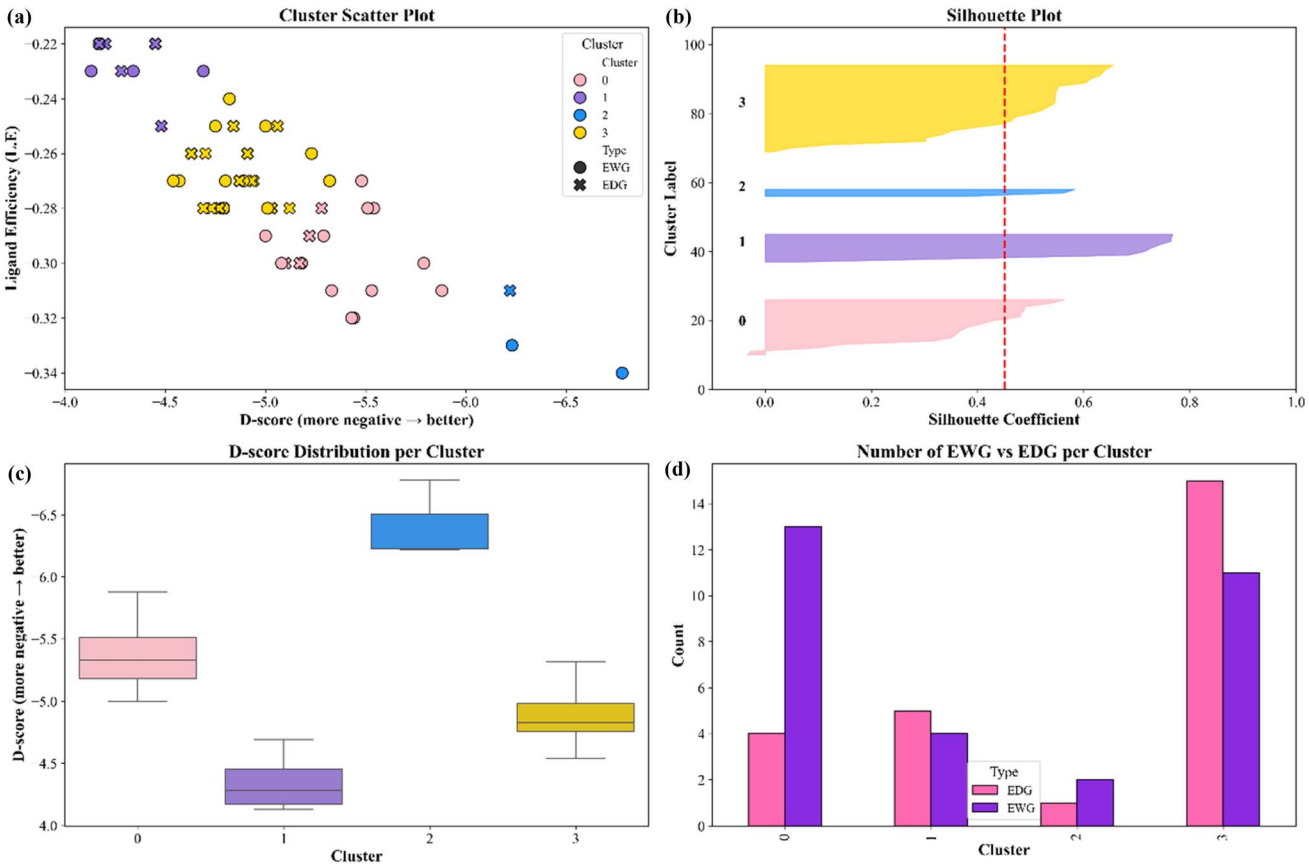

Fig. 4 Clustering analysis of sulfamethoxazole derivatives based on *D*-score and ligand efficiency. (a) Scatter plot of *D*-score *vs.* ligand efficiency colored by KMeans clusters, (b) silhouette plot for cluster quality assessment, (c) boxplot of *D*-score distribution per cluster, (d) counts of EWG *vs.* EDG derivatives per cluster.

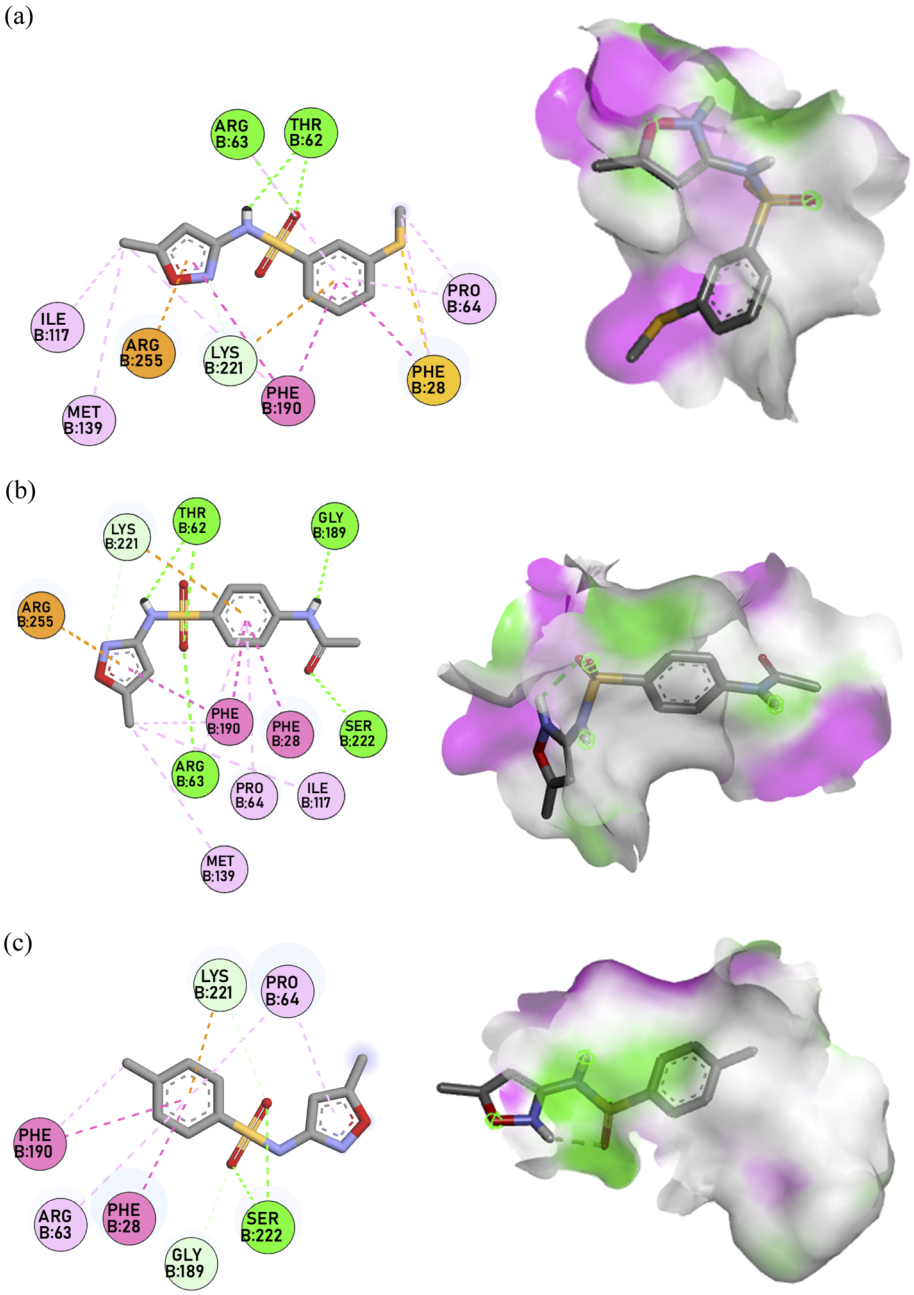

Fig. 5 (a) 2D and 3D interaction diagrams of the docked **SMX053** within the binding pocket of DHPS protein, showing key hydrogen bonds, hydrophobic interactions, and other non-covalent interactions with surrounding residues. (b) 2D and 3D interaction diagrams of the docked **SMX051** within the binding pocket of DHPS protein, showing key hydrogen bonds, hydrophobic interactions, and other non-covalent interactions with surrounding residues. (c) 2D and 3D interaction diagrams of the docked **SMX033** within the binding pocket of DHPS protein, showing key hydrogen bonds, hydrophobic interactions, and other non-covalent interactions with surrounding residues.

and pi-cation contacts with Lys^{221} and Arg^{255}. The strategic recruitment of Arg^{255}, a residue essential for pterin-site recognition, may synergize with hydrogen bond interactions involving Thr^{62}, Arg^{63}, and Pro^{64} to enhance stability.[50] This binding strategy follows the substrate envelope principle by confining interactions within the native volume of *p*-aminobenzoic acid (PABA), thus avoiding mutation-prone regions (*e.g.*, Phe^{33}, Pro^{69}, Thr^{67}).[51] By utilizing the phylogenetically conserved Arg^{255}, this approach connects the PABA and pterin sites, leading to a hybrid inhibitory mechanism that is less prone to single-point mutations (Table 3).[52]

MMGBSA is a computationally efficient method that combines molecular mechanics energies for both protein and ligand atoms with solvation terms derived from the Generalized Born model.[53] This approach was utilized to refine the docking poses and served as an additional selection criterion to advance the designed compounds to the next stage. Following MMGBSA refinement in the PRIME module, twenty-four (24) derivatives

Table 3 Docking scores (*D*-scores) and ligand efficiencies (L.E.) of sulfamethoxazole (SMX) derivatives against DHPS

Compound	Substituent (position)	Type	Relative strength	*D*-Score	L.E.
SMX	*p*-Amino	EDG	Very strong	−4.79	−0.28
SMX001	*o*-Nitro	EWG	Strong	−4.17	−0.22
SMX002	*m*-Nitro	EWG	Strong	−4.75	−0.25
SMX003	*p*-Nitro	EWG	Strong	−4.34	−0.23
SMX004	*o*-Cyano	EWG	Strong	−4.13	−0.23
SMX005	*m*-Cyano	EWG	Strong	−5.01	−0.28
SMX006	*p*-Cyano	EWG	Strong	−5.53	−0.31
SMX007	*o*-Trifluoromethyl	EWG	Strong	−5	−0.25
SMX008	*m*-Trifluoromethyl	EWG	Strong	−5.54	−0.28
SMX009	*p*-Trifluoromethyl	EWG	Strong	−4.69	−0.23
SMX010	*o*-Carboxylic acid	EWG	Moderate	−6.23	−0.33
SMX011	*m*-Carboxylic acid	EWG	Moderate	−5.79	−0.3
SMX012	*p*-Carboxylic acid	EWG	Moderate	−5.88	−0.31
SMX013	*o*-Methyl ester	EWG	Moderate	−5.32	−0.27
SMX014	*m*-Methyl ester	EWG	Moderate	−5.51	−0.28
SMX015	*p*-Methyl ester	EWG	Moderate	−4.82	−0.24
SMX016	*o*-Sulfonic acid	EWG	Strong	−5.48	−0.27
SMX017	*m*-Sulfonic acid	EWG	Strong	−5.23	−0.26
SMX018	*p*-Sulfonic acid	EWG	Strong	−6.78	−0.34
SMX019	*o*-Bromo	EWG	Weak	−5.18	−0.3
SMX020	*m*-Bromo	EWG	Weak	−5.08	−0.3
SMX021	*p*-Bromo	EWG	Weak	−5.44	−0.32
SMX022	*o*-Chloro	EWG	Weak	−4.79	−0.28
SMX023	*m*-Chloro	EWG	Weak	−5	−0.29
SMX024	*p*-Chloro	EWG	Weak	−5.33	−0.31
SMX025	*o*-Fluoro	EWG	Weak	−4.57	−0.27
SMX026	*m*-Fluoro	EWG	Weak	−5.43	−0.32
SMX027	*p*-Fluoro	EWG	Weak	−4.54	−0.27
SMX028	*o*-Formyl	EWG	Strong	−4.8	−0.27
SMX029	*m*-Formyl	EWG	Strong	−5.29	−0.29
SMX030	*p*-Formyl	EWG	Strong	−4.89	−0.27
SMX031	*o*-Methyl	EDG	Weak	−4.79	−0.28
SMX032	*m*-Methyl	EDG	Weak	−4.73	−0.28
SMX033	*p*-Methyl	EDG	Weak	−4.77	−0.28
SMX034	*o*-Methoxy	EDG	Strong	−5.03	−0.28
SMX035	*m*-Methoxy	EDG	Weak	−5.12	−0.28
SMX036	*p*-Methoxy	EDG	Strong	−4.63	−0.26
SMX037	*o*-Hydroxy	EDG	Strong	−5.17	−0.3
SMX038	*m*-Hydroxy	EDG	Weak	−5.1	−0.3
SMX039	*p*-Hydroxy	EDG	Strong	−4.69	−0.28
SMX040	*o*-Methylamino	EDG	Strong	−4.87	−0.27
SMX041	*m*-Methylamino	EDG	Weak	−4.7	−0.26
SMX042	*p*-Methylamino	EDG	Strong	−5.22	−0.29
SMX043	*o*-Dimethylamino	EDG	Very strong	−4.91	−0.26
SMX044	*m*-Dimethylamino	EDG	Weak	−4.84	−0.25
SMX045	*p*-Dimethylamino	EDG	Very strong	−4.2	−0.22
SMX046	*o*-Ethoxy	EDG	Strong	−4.17	−0.22
SMX047	*m*-Ethoxy	EDG	Weak	−5.28	−0.28
SMX048	*p*-Ethoxy	EDG	Strong	−4.28	−0.23
SMX049	*o*-Acetamido	EDG	Moderate	−5.06	−0.25
SMX050	*m*-Acetamido	EDG	Moderate	−6.22	−0.31
SMX051	*p*-Acetamido	EDG	Moderate	−4.45	−0.22
SMX052	*o*-Methylthio	EDG	Moderate	−4.93	−0.27
SMX053	*m*-Methylthio	EDG	Moderate	−4.94	−0.27
SMX054	*p*-Methylthio	EDG	Moderate	−4.48	−0.25

progressed to the next phase of computational profiling (Table 4). These derivatives exhibited superior MM-GBSA binding energies against DHPS compared to sulfamethoxazole (SMX: −45.03 kcal mol^{-1}), thereby confirming the effectiveness of substitution strategies across various chemical classes. High-affinity compounds included derivatives featuring electron donating groups (*e.g.*, **SMX051**: −58.46 kcal mol^{-1}), electron-withdrawing groups (*e.g.*, **SMX018**: −49.62, **SMX023**: −49.35, **SMX033**: −47.86 kcal mol^{-1}), and polar functionalities (*e.g.*, **SMX050**: −49.68 kcal mol^{-1}).

Table 4 Energy decomposition analysis of SMX derivatives against DHPS

Derivative	Bind	Coulomb	Covalent	Hbond	Lipo	Packing	Solv_GB	vdW
SMX	−45.03	−21.71	3.26	−2.95	−9.82	−3.98	24.36	−34.18
SMX005	−46.93	−19.81	2.28	−1.09	−9.72	−1.23	19.48	−36.82
SMX010	−47.24	−35.96	3.31	−2.07	−9.15	−0.94	29.28	−31.71
SMX012	−47.66	−28.35	2.82	−2.74	−9.79	−2.33	26.67	−33.94
SMX015	−45.86	−15.39	2.53	−2.16	−10.76	−2.44	21.86	−39.49
SMX017	−46.96	−26.88	3.85	−1.54	−8.76	−1.11	24.52	−37.03
SMX018	−49.62	−25.01	2.57	−2.62	−8.73	−2.75	21.79	−34.86
SMX020	−46.24	−21.66	2.97	−2.15	−10.82	−1.99	21.78	−34.38
SMX023	−49.35	−27.66	3.01	−2.17	−12.92	−3.92	30.58	−36.28
SMX024	−46.12	−21.79	2.98	−2.47	−13.07	−4.14	25.75	−33.39
SMX026	−45.54	−27.88	3	−2.18	−11.57	−3.95	30.83	−33.77
SMX029	−49.17	−31.5	3.99	−2.89	−10.15	−3.88	33.52	−38.25
SMX030	−47.51	−32.69	3.33	−2.68	−10.25	−4.12	33.39	−34.48
SMX032	−47.01	−20.31	3.03	−2.19	−13.09	−3.93	25.26	−35.78
SMX033	−47.86	−9.19	0.12	−1.43	−12.61	−1.41	11.55	−34.89
SMX035	−45.45	−21.53	2.75	−2.24	−12.87	−3.97	29.83	−37.41
SMX037	−45.46	−24.98	0.31	−1.34	−8.85	−0.89	19.21	−28.92
SMX038	−46.21	−25.92	3.25	−2.32	−11.62	−4.02	28.28	−33.86
SMX041	−48.43	−22.47	3.46	−2.28	−12.99	−4.01	27.05	−37.18
SMX042	−46.89	−21.07	3.21	−2.94	−10.85	−3.99	25.82	−37.07
SMX044	−45.53	−10.35	0.95	−1.46	−12.85	−0.97	14.37	−35.21
SMX047	−49.28	−18.47	3.73	−2.16	−12.75	−2.06	22.54	−40.11
SMX050	−49.68	−32.27	7.06	−3.11	−11.44	−3.97	35.22	−41.16
SMX051	−58.46	−43.82	5.1	−3.58	−11.15	−3.97	40.32	−41.36
SMX053	−50.59	−26.91	5.73	−2.12	−13.11	−3.89	30.82	−41.1

The differences in the MMGBSA binding free energy between sulfamethoxazole and the filtered derivatives indicated that the derivatives fit better into the DHPS binding pockets or adjacent binding clefts. This improved fit creates strong polar and nonpolar contacts with the active site residues, effectively holding the derivatives within the binding site or in allosteric clefts.[54] The successful candidates exhibited high positive solvation energy values, implying a desolvation penalty upon binding; however, this penalty was outweighed by the strong van der Waals interactions and coulombic energies. The performance of the top binders was attributed to their coulombic energy and favourable van der Waals forces, which are significantly more advantageous than those of sulfamethoxazole. This evidence suggests that the successful derivatives enhance the formation of stronger salt bridges, dipole–dipole interactions, or charge-assisted hydrogen bonds and van der Waals contact with the DHPS active site. It also implies that modifications improving electrostatic fit without compromising van der Waals contacts are likely to achieve better binding to the DHPS protein target.[55] The free binding energies from the simulation further confirmed the strength of ligand binding to the target and their favorable interactions with DHPS, as evidenced by the docking studies.

Derivatives that exhibited superior MMGBSA scores compared to sulfamethoxazole were selected for molecular docking and MMGBSA calculations with the LasR and AcrB proteins. In the context of quorum-sensing inhibition, the top 24 DHPS-targeting derivatives were evaluated against *Pseudomonas aeruginosa* LasR. While sulfamethoxazole (SMX) demonstrated an MMGBSA score of −43.30 kcal mol^{-1}, 17 derivatives displayed enhanced binding free energies (dBind), particularly **SMX018** (−52.81 kcal mol^{-1}) and **SMX047** (−51.10 kcal mol^{-1}). Docking analysis indicated competitive displacement of the autoinducer 3-oxo-C12-HSL through hydrogen bonding with residues including Thr^{115}, Ser^{129}, Thr^{75}, Tyr^{56}, Leu^{39}, and Gly^{38}. Additional interactions included π–π stacking with Tyr^{64}, pi-sulfur interactions with Asp^{73}, and hydrophobic interactions with Val^{76}, Leu^{125}, Ala^{127}, Leu^{40}, Leu^{36}, and Ala^{50} as illustrated in Fig. 6a–d.

Moreover, these derivatives caused allosteric disruption by occupying the Ile^{52}–Ala^{50} hydrophobic subpocket, which impaired dimerization and DNA binding, resembling the mechanism of phage protein Aqs1.[56] The incorporation of halogen atoms in compounds such as **SMX019** and **SMX020** enhanced potency *via* halogen bonding (*e.g.*, with Val^{76}) and hydrophobic filling of subpockets. Structure–activity relationships suggested that optimal hydrophobic rings were essential for acyl pocket occupation, with increased rigidity leading to reduced entropic penalties and improved hydrogen bonding with the sulphonamide functional group.[57] Biologically, these derivatives can disrupt the LasR-RhlR-PQS hierarchy, thereby inhibiting virulence factors such as elastase and pyocyanin.

For efflux pump inhibition, the derivatives were evaluated against *E. coli* AcrB. SMX exhibited a free binding energy of −34.17 kcal mol^{-1}, while 7 derivatives showed improved affinity. The derivatives target the periplasmic vestibule, engaging Phe^{664} and Pro^{669} (Fig. 7a–d), which are critical for van der Waals interactions with native substrates such as deoxycholate, ciprofloxacin, and ethidium. Notably, deoxycholate binds in the same vestibule region and forms a hydrogen bond

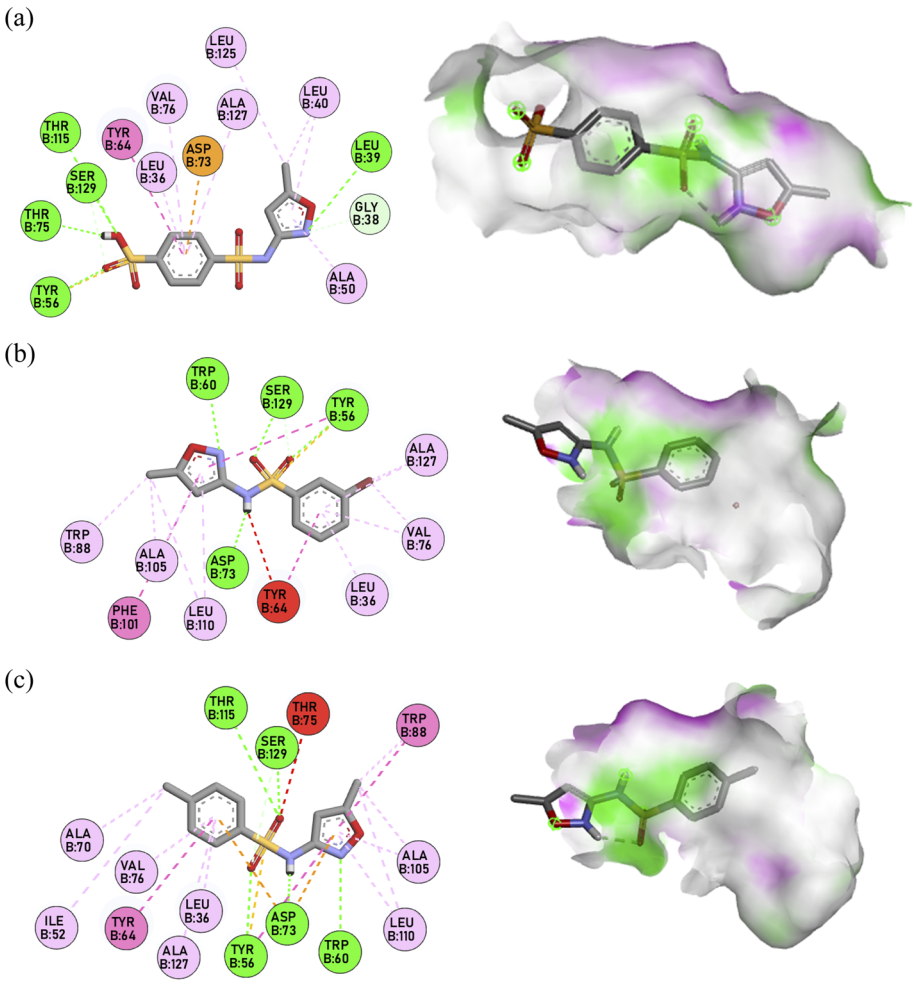

Fig. 6 (a) 2D and 3D interaction diagrams of the docked **SMX018** within the binding pocket of LasR (PDB ID: 6v7x) protein, showing key hydrogen bonds, hydrophobic interactions, and other non-covalent interactions with surrounding residues. (b) 2D and 3D interaction diagrams of the docked **SMX020** within the binding pocket of LasR (PDB ID: 6v7x) protein, showing key hydrogen bonds, hydrophobic interactions, and other non-covalent interactions with surrounding residues. (c) 2D and 3D interaction diagrams of the docked **SMX033** within the binding pocket of LasR (PDB ID: 6v7x) protein, showing key hydrogen bonds, hydrophobic interactions, and other non-covalent interactions with surrounding residues.

with Ser^{715}, in addition to hydrophobic interactions with Phe^{664},[58] supporting the biological relevance of this site. Novel interactions include hydrogen bonds with Arg^{717} (unused by ciprofloxacin/ethidium), creating a steric block at the vestibule entrance.[1,4] Pi–sulfur bonds with Met^{575} and hydrogen bonds with Pro^{718}, Gly^{720}, Asn^{719}, Ala^{665}, Asn^{667}, Met^{649}, Thr^{648}, Thr^{678}, and Gln^{830} further enhance entropy to counter vestibule flexibility.[58]

Mechanistically, vestibule confinement arrests AcrB in the "loose" (L) state, as was observed in the deoxycholate-bound AcrB structure, preventing rotational transition to export-competent conformations ("tight"/"open" states).

Following the computational modeling, five derivatives (**SMX001**, **SMX003**, **SMX015**, **SMX019**, and **SMX033**) were prioritized for synthesis and biological evaluation. This selection was designed to rigorously validate our computational predictions and probe critical structure–activity relationships. Specifically, **SMX001** and **SMX003** tested the hypothesis that electron-withdrawing groups enhance binding affinity to DHPS. **SMX015** was chosen to evaluate whether incorporating polar functionality enabled high-affinity dual engagement with both DHPS and LasR targets. To probe the predicted role of halogen bonding in LasR inhibition, **SMX019** was selected. Finally, **SMX033** served as a critical benchmark for ADME/toxicity, boasting a favorable predicted solubility and safety profile, in addition to its strong van der Waals contacts within AcrB's hydrophobic vestibule.

6.1.3 Design strategy and chemistry of the sulfamethoxazole derivatives. A small library of five sulfamethoxazole derivatives was synthesized by a pH-dependent reaction between 3-amino-5-methylisoxazole and sulphonyl chlorides 30 (Fig. 8). The progress of the reaction was monitored using aluminum-coated backing silica gel TLC plates. After purification by silica column chromatography with a mobile phase of CH_2Cl_2 (dichloromethane) : Et_2O (diethyl ether) [60 : 40], all corresponding sulfamethoxazole derivatives were obtained in 65–78% yields (Fig. 8 and Table 5).

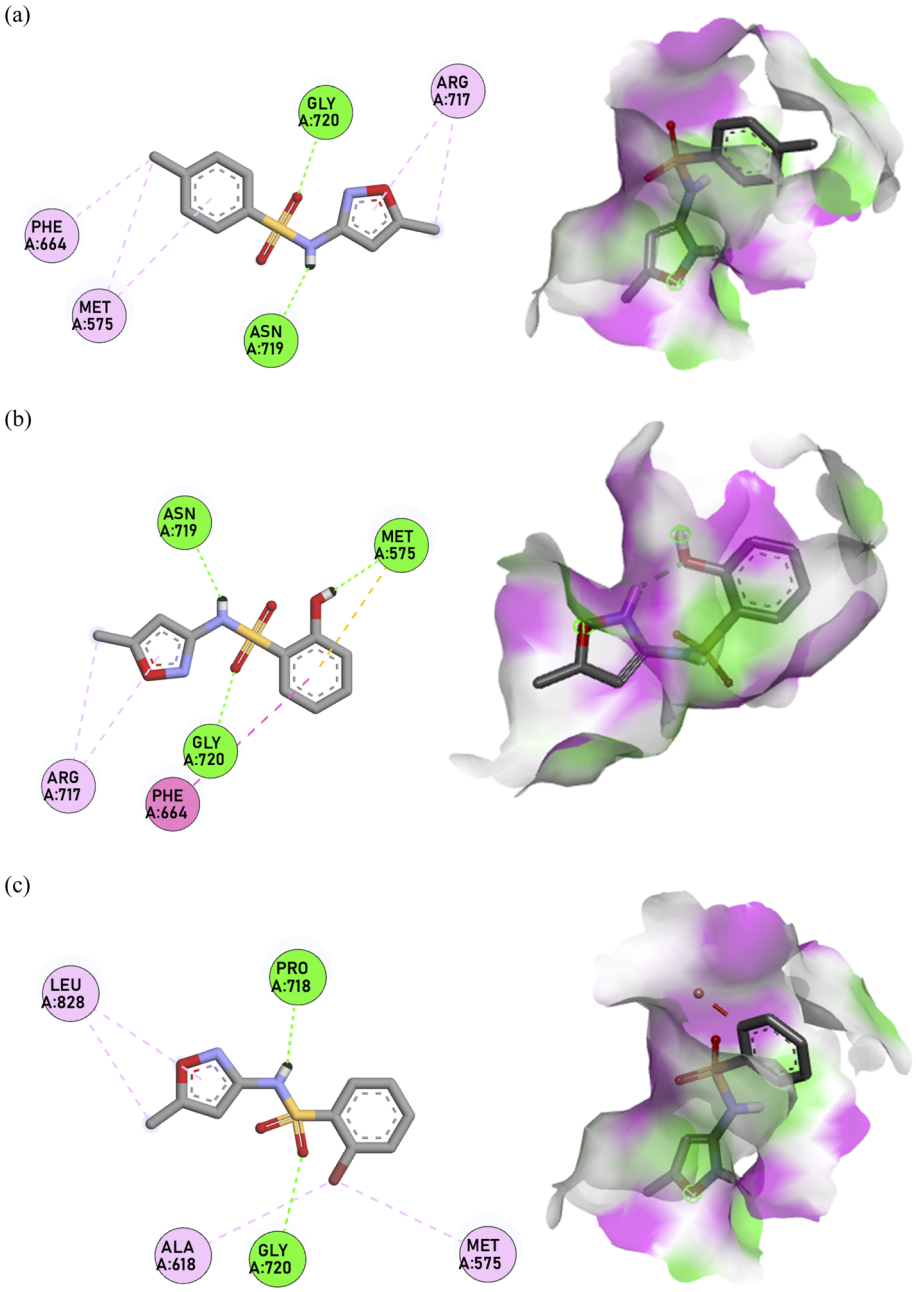

Fig. 7 (a) 2D and 3D interaction diagrams of the docked **SMX033** within the binding pocket of AcrB (PDB ID: 2w1b) protein, showing key hydrogen bonds, hydrophobic interactions, and other non-covalent interactions with surrounding residues. (b) 2D and 3D interaction diagrams of the docked **SMX037** within the binding pocket of AcrB (PDB ID: 2w1b) protein, showing key hydrogen bonds, hydrophobic interactions, and other non-covalent interactions with surrounding residues. (c) 2D and 3D interaction diagrams of the docked **SMX019** within the binding pocket of AcrB (PDB ID: 2w1b) protein, showing key hydrogen bonds, hydrophobic interactions, and other non-covalent interactions with surrounding residues.

The compounds were confirmed by their structures using ^{1}H NMR, ^{13}C NMR spectroscopy and HRMS. The ^{1}H NMR spectrum of compound **SMX033** showed a broad peak between 6.24 and 6.26 ppm, indicating the formation of the sulfonamide group. The doublet peaks observed downfield at 7.68 to 7.70 ppm correspond to the *p*-disubstituted sulfonyl aromatic portion. The HRMS analysis revealed the molecular ion peak calculated for $[M + H]^{+}$ as 252.0569, while the observed peak was 253.0649. Based on the structural evaluation, compound **SMX033** was designated as 4-methyl-*N*-(5-methylisoxazol-3-yl)benzenesulfonamide. The primary amino group of sulfamethoxazole was converted through synthesis to generate compounds with electron-withdrawing and donating groups on the benzene sulfonyl portion, which were synthesized in good to excellent yields (60–78%).

6.1.4 Biological evaluation

6.1.4.1 Minimum inhibitory concentration (MIC) and cytotoxicity. The MICs of the synthesized compounds against test

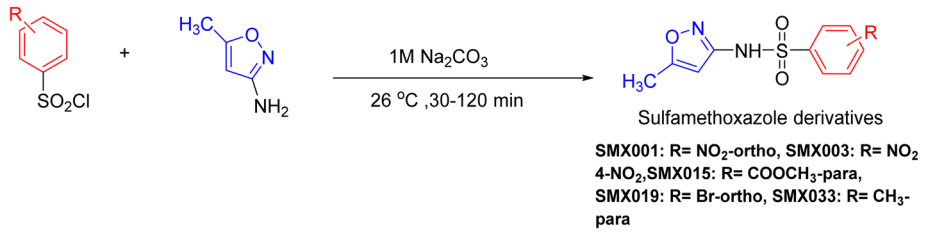

Fig. 8 Scheme for the synthesis of the substituted sulfamethoxazole.

Table 5 Physicochemical characterisation data of the synthesised compounds

Compound	–R	Molecular formula	Calculated molecular weight	Melting point (°C)	Yield (%)
SMX001	*o*-NO_2	$C_{10}H_9N_3O_5S$	283.03	116–118	78
SMX003	*p*-NO_2	$C_{10}H_9N_3O_5S$	283.03	118–120	71
SMX015	*p*-$COOCH_3$	$C_{11}H_{12}N_2O_3S$	296.06	126–129	75
SMX019	*o*-Br	$C_{10}H_9BrN_2O_3S$	315.95	164–167	75
SMX033	*p*-CH_3	$C_{11}H_{12}N_2O_3S$	252.06	125–127	65

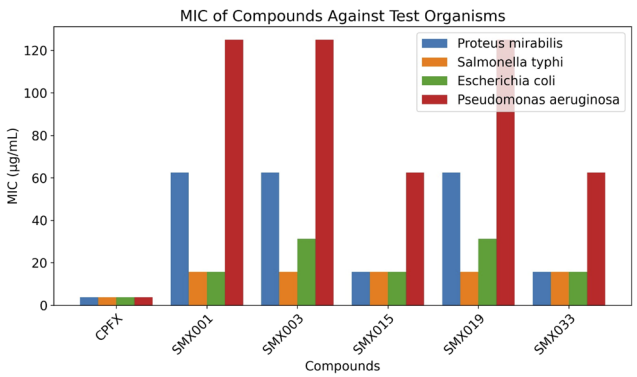

Fig. 9 Minimum inhibitory concentrations (MICs) of SMX derivatives against ESKAPE pathogens.

organisms (*Proteus mirabilis*, *Salmonella typhi*, *Escherichia coli*, and *Pseudomonas aeruginosa*) were determined using the broth microdilution technique. Fig. 9 shows the MIC values of the compounds within the range of 15.625 to 125 μg mL^{-1}. All the synthesized derivatives exhibited MIC values <100 μg mL^{-1} against the test organisms, except *Pseudomonas aeruginosa*, which showed MIC values >100 μg mL^{-1} for **SMX001**, **SMX003**, and **SMX019**. The cytotoxicity data on the compounds is shown in Table 6.

The *in vitro* antibiotic potential of the five (5) sulfamethoxazole derivatives was assessed individually using the high-throughput spotting assay method. The MIC of the five (5) synthesized compounds was determined alongside ciprofloxacin and DMSO as positive and negative controls, respectively. All compounds showed significant antibacterial activity against *P. mirabilis*, *S. typhi*, and *E. coli* (MICs 15.625–62.5 μg mL^{-1}), although they were less potent than ciprofloxacin (3.91 μg mL^{-1}). Compounds **SMX015** and **SMX033** demonstrated high inhibitory activity against *P. mirabilis*, *S. typhi*, and *E. coli* (MIC: 15.625 μg mL^{-1}). Compounds **SMX001**, **SMX003**, and **SMX019** recorded inhibitory activity against *S. typhi* (MIC: 15.625 μg mL^{-1}). Additionally, compound **SMX001** also recorded inhibitory activity (MIC: 15.625) against *E. coli*. Activity against the more resistant *Pseudomonas aeruginosa* was markedly reduced (MICs 62.5–125 μg mL^{-1}) compared to ciprofloxacin (3.91 μg mL^{-1}), indicating substantial intrinsic resistance. Compound

Table 6 MIC of susceptible organisms and cytotoxicity comparison data of the synthesised compounds

Compound	–R	Molecular formula	[a]MIC (μg mL^{-1}) ± SEM	[b]CC_{50} (μM) ± SEM	SI[c]
SMX001	*o*-NO_2	$C_{10}H_9N_3O_5S$	441.00 ± 0.050	112.22 ± 0.060	0.25
SMX003	*p*-NO_2	$C_{10}H_9N_3O_5S$	441.00 ± 0.002	125 ± 0.060	0.28
SMX015	*p*-$COOCH_3$	$C_{11}H_{12}N_2O_3S$	61.98 ± 0.060	186.00 ± 0.005	3.00
SMX019	*o*-Br	$C_{10}H_9BrN_2O_3S$	395.63 ± 0.025	121.10 ± 0.060	0.30
SMX033	*p*-CH_3	$C_{11}H_{12}N_2O_3S$	61.98 ± 0.020	286.20 ± 0.001	4.62
Ciprofloxacin	—	$C_{17}H_{18}FN_3O_3$	3.91 ± 0.0001	Not deterermined	—

[a] MIC: minimum inhibitory concentration of compounds **SMX015** and **SMX033** demonstrating highest inhibitory activity against *P. mirabilis*, *S. typhi*, and *E. coli* (MIC: 15.625 μg mL^{-1}). [b] CC_{50} = 50% cytotoxic concentration on Vero cells. [c] SI = selective index (CC_{50}/MIC); ciprofloxacin positive control. [a]IC_{50} and [b]CC_{50} values represent triplicate determinations (three determinations from three different experiments).

SMX033 features a methyl group at the *para* position, whilst compounds **SMX015** and **SMX001** feature *p*-methyl ester and *o*-nitro groups, respectively. **SMX033** demonstrated comparable or improved activity relative to sulfamethoxazole against most tested Gram-negative pathogens. Compound **SMX033** consistently demonstrated significant antibacterial activity against all tested pathogens, suggesting its potential as a broad-spectrum agent. *Pseudomonas aeruginosa*, the most resistant pathogen, was susceptible to **SMX033** and **SMX019** at 62.5 μg mL^{-1} and **SMX001**, **SMX003**, and **SMX015** MIC at 125 μg mL^{-1}, indicating moderate inhibition. The observed MIC values (15.625–125 μg mL^{-1}) against Gram-negative pathogens align with the computational ranking based on MMGBSA binding free energies. Notably, **SMX033** (*p*-CH_3) and **SMX015** (*p*-$COOCH_3$) consistently exhibited the lowest MICs (most potent activity), particularly against *P. mirabilis*, *S. typhi*, and *E. coli* (15.625 μg mL^{-1}). Their strong computational scores directly support this strong inhibitory activity. **SMX033** showed favourable MM-GBSA scores relative to the parent compound for each target individually. Its high affinity, predicted to stem from optimal van der Waals contacts in the hydrophobic vestibules of AcrB and LasR, translates to effective bacterial growth inhibition by simultaneously disrupting folate synthesis, quorum sensing, and efflux. The potent activity of **SMX015** aligns with its *in silico* profile, where it ranked among the top compounds for affinity against DHPS, LasR and AcrB in separate MM-GBSA calculations. Its polar ester group was predicted to facilitate dual engagement, which is consistent with its potent and broad-spectrum MIC results.[59] The reduced activity against *P. aeruginosa* (MICs: 62.5–125 μg mL^{-1}) for all compounds was anticipated. This pathogen possesses a notoriously impermeable outer membrane and highly efficient efflux systems, which our *in silico* models, focused on target binding, would not fully account for. *P. aeruginosa* is highly resistant and could require different derivatives or scaffolds.[60] However, the fact that **SMX033** and **SMX015** still showed the best activity (MIC = 62.5 μg mL^{-1}) against this resilient pathogen underscores the strength of the multi-target approach, as overcoming its defence likely requires potent inhibition of multiple resistance pathways simultaneously.[61] Compound **SMX033** is arguably the most potent when compared with ciprofloxacin because the substitution of the methyl in the phenyl ring present at the *para* position of the isoxazole nucleus enhanced the antimicrobial activity and decreased the cytotoxic activity of compound **SMX033**. Compound **SMX033** exhibited reduced cytotoxicity against Vero cell lines, with a CCC_{50} value of 286.20 μM suggesting its high selectivity towards the pathogens.

6.1.4.2 Biofilm formation inhibition. Biofilms are structured communities of microorganisms embedded in an extracellular matrix, offering protection against antimicrobials.[62] The ability to inhibit biofilm formation is critical for treating chronic infections, as biofilms are notoriously resistant to conventional antibiotics. By preventing biofilm development, the compounds could reduce microbial persistence and improve treatment outcomes. Biofilm inhibition might result from interference with adhesion, quorum sensing, or EPS synthesis.[62–64] Biofilm formation inhibition effects of the compounds **SMX033**, **SMX019**, **SMX003**, **SMX015**, and **SMX001** at sub-MIC concentrations against *Proteus mirabilis*, *Salmonella typhi*, *Escherichia coli*, and *Pseudomonas aeruginosa* were analysed and represented in Fig. 10a and b. The antibiotic's subminimal inhibitory concentration (sub-MIC) can influence the biofilm formation capacity of bacterial pathogens, thereby impacting the pathogenesis and infection outcomes.[65] The compounds exhibited excellent biofilm inhibition. All derivatives, particularly **SMX033**, **SMX015**, and **SMX001**, achieved exceptional inhibition (>98.5%) against the tested organisms, significantly outperforming the parent drug ciprofloxacin (94.35) (Fig. 10a and b). This result directly correlates with the molecular docking predictions. Our models indicated that these derivatives competitively displace the native autoinducer (OHN) in the LasR binding pocket by forming key hydrogen bonds with residues Thr^{75}, Tyr^{56}, and Ser^{129}. Furthermore, they were predicted to cause allosteric disruption by occupying the critical Ile^{52}–Ala^{50} hydrophobic subpocket, impairing LasR dimerization and DNA binding, a mechanism known to inhibit biofilm formation profoundly.[66] The superior experimental biofilm inhibition of **SMX019** (*o*-Br) against *E. coli* aligns with its *in silico* prediction of enhanced potency through halogen bonding (*e.g.*, with Val^{76} in LasR). The strong experimental biofilm inhibition across the board confirms the computational prediction that targeting LasR is a viable and effective strategy for these sulfamethoxazole derivatives.

Absorbance reflects remaining biofilm biomass, where lower values indicate greater inhibition.[67] Each value is the average of replicate readings for three determinations with their standard deviation (SD). The negative control, which contained no antimicrobial treatment, served as a baseline for maximum biofilm formation in the organism.

6.1.4.3 Ethidium bromide efflux pump inhibition assay. Efflux pumps are membrane proteins found in bacteria that actively expel toxic substances including antibiotics out of the pathogen cell.[68] Some of these efflux pumps are non-specific, removing a wide range of drug molecules, while others are selective. Efflux pump inhibitors are compounds that block the activity of these pumps, thereby increasing the intracellular concentration of antibiotics and restoring their effectiveness.[69] The relevance of efflux pump inhibition still remains intact as it aids in combating antibiotic resistance. Overexpression of efflux pumps is a common mechanism of multidrug resistance, especially in pathogens like *Pseudomonas aeruginosa*, *Escherichia coli*, and *Acinetobacter baumannii*.[70] Efflux pump inhibitors (EPIs) enhance drug potency by retaining antibiotics inside bacteria cells, thereby lowering the required dose of antibiotic and reducing side effects. Combining an antibiotic (even older and less tolerated drugs) with EPIs can offer a synergistic effect.[71,72] Ethidium bromide was utilized in the evaluation of the efflux pump inhibition potential of the compounds. Because it may intercalate DNA, which breaks down DNA structure and causes cell death, the dye ethidium bromide (EB) possesses antibiotic activity.[73] The efflux pump is the sole defense mechanism that bacteria use to fend off the effects of ethidium bromide.[74] This method has been used in many studies to investigate the presence or absence of efflux pumps in

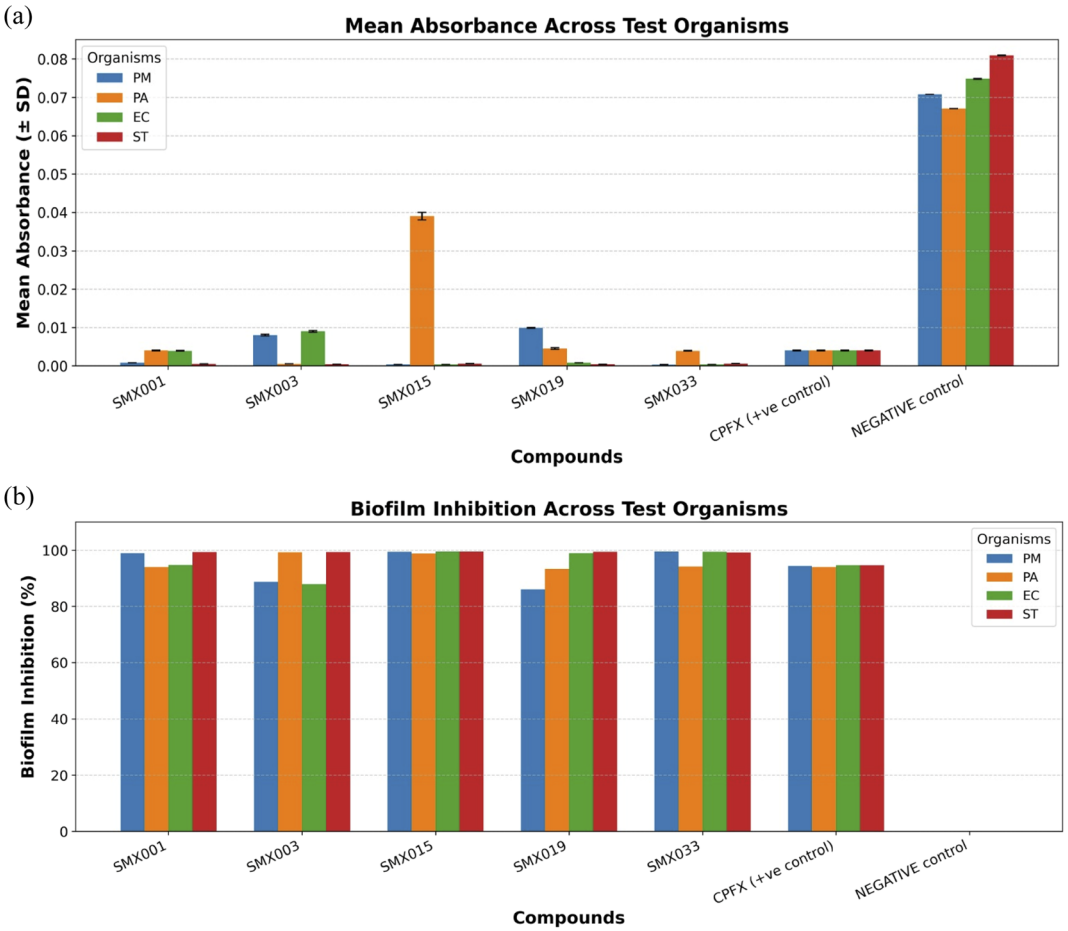

Fig. 10 (a) Mean absorbance of SMX derivatives. (b) Biofilm inhibition of derivatives against test organisms. All derivatives achieved exceptional biofilm inhibition (>99%) against *Salmonella typhi* compared to ciprofloxacin (94.35%); compounds **SMX033**, **SMX015**, and **SMX001** demonstrated excellent biofilm inhibition (>98.5%) against *Proteus mirabilis*; and **SMX033**, **SMX015**, and **SMX019** also showed excellent biofilm inhibition (>98%) against, *Escherichia coli*. Compared to ciprofloxacin, the derivatives performed significantly.

combination with traditional efflux pump inhibitors.[75,76] To evaluate the compound's effectiveness, the efflux pump inhibition experiment used ethidium bromide (EtBr) as a substrate. The premise of this experiment is that EtBr has strong intracellular fluorescence. As it keeps building up, it binds to DNA and creates a growing fluorescence. When they build up inside the bacterial cells, the fluorescence intensity rises, indicating that the efflux pump mechanism is being inhibited. A low fluorescence measurement occurs when the cell pumps out EtBr in the absence of efflux pump inhibitory action. The fluorescence intensity was recorded at an interval of everyone (1) minute for a total period of sixty (60)-minutes (Fig. 11a–d). Compound **SMX033** (CH_3-*para*) demonstrated a remarkable inhibition of the efflux pump and was the strongest EPI overall.

SMX033 was predicted to bind strongly in the periplasmic vestibule of AcrB, interacting with key residues such as Phe[664] and Pro[669] through significant van der Waals and hydrophobic interactions. The methyl group at the para position was computationally identified as essential for occupying the hydrophobic pocket formed by Phe[664], a residue crucial for substrate binding and expulsion. By obstructing this vestibule, **SMX033** is expected to stabilize AcrB in the "loose" (L) state, thereby preventing the conformational changes necessary for antibiotic export. The experimental observation of high ethidium bromide (EtBr) accumulation serves as direct functional evidence of this mechanism.[77] Additionally, the moderate to satisfactory efflux pump inhibitor (EPI) activity of **SMX015**, **SMX019**, **SMX003**, and **SMX001** correlates with their *in silico* profiles. Their diverse substituents (ester, bromo, and nitro) were anticipated to interact with the vestibule through different mechanisms, such as forming hydrogen bonds with Arg[717] or pi–sulfur interactions with Met[575], which explains their measurable, albeit lower, efflux inhibition compared to **SMX033**.[78,79]

7 Molecular dynamics simulation studies

To complement the molecular docking analyses and provide a dynamic validation of the binding stability and conformational effects induced by the prioritized sulfamethoxazole derivatives, molecular dynamics (MD) simulations of 100 ns

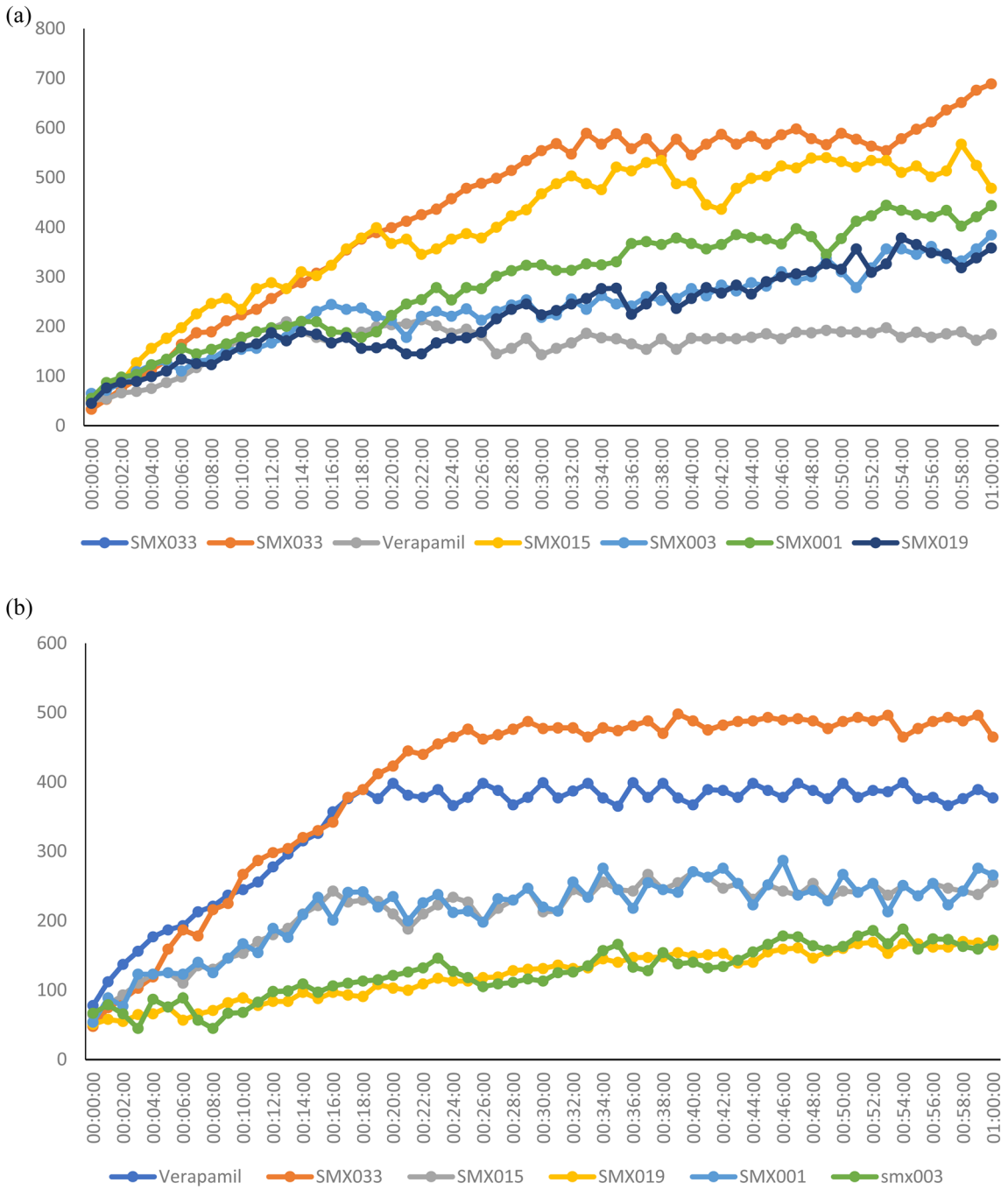

Fig. 11 (a) Time-dependent efflux pump inhibition in *Escherichia coli* by verapamil and sulfamethoxazole derivatives. (b) Time-dependent efflux pump inhibition in *Pseudomonas aeruginosa* by verapamil and sulfamethoxazole derivatives. (c) Time-dependent efflux pump inhibition in *Proteus mirabilis* by verapamil and sulfamethoxazole derivatives. (d) Time-dependent efflux pump inhibition in *Salmonella typhi* by verapamil and sulfamethoxazole derivatives.

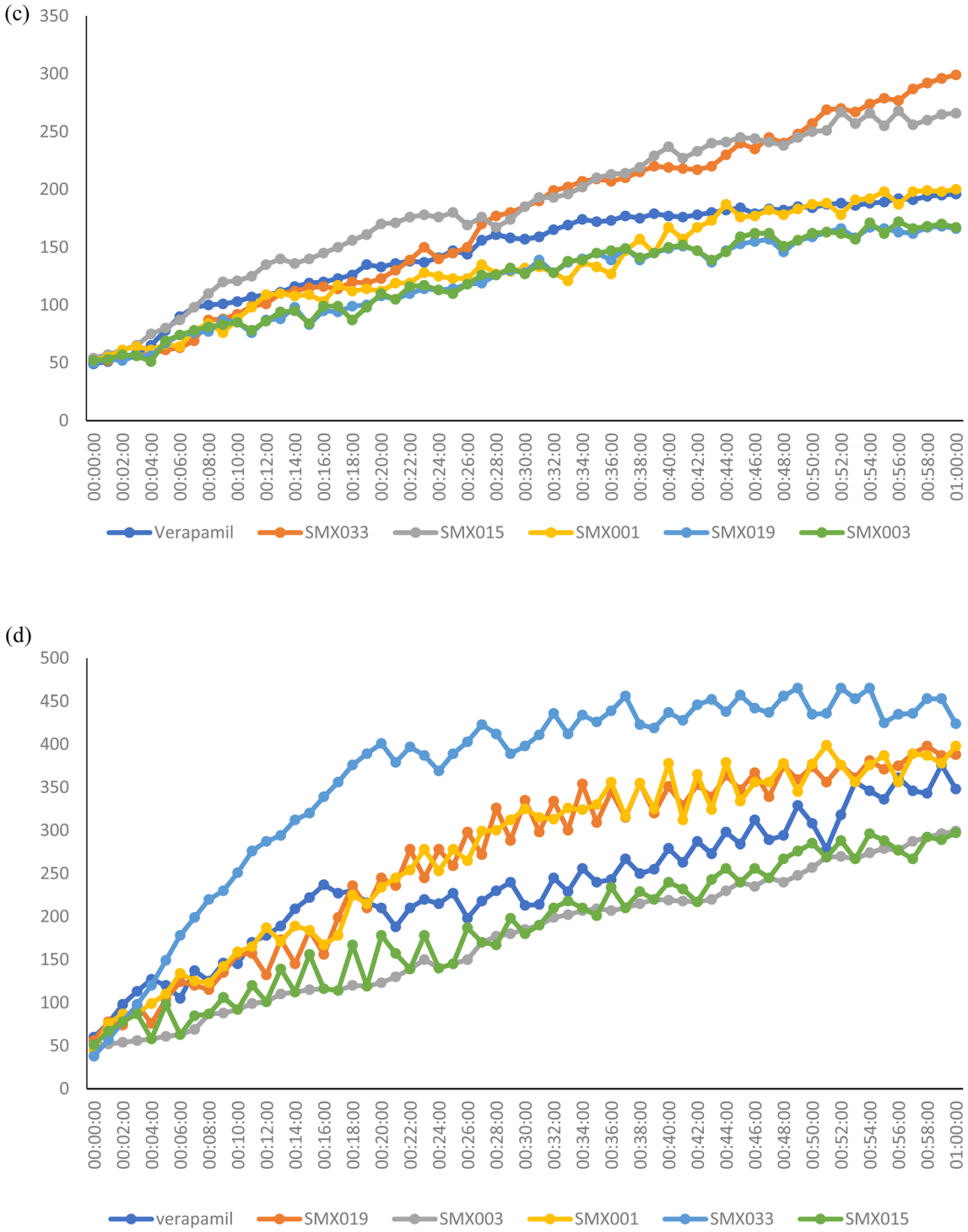

Fig. 11 *cont.*

duration were performed. The top two candidates, **SMX033** and **SMX015**, were simulated in complex with the primary enzyme target dihydropteroate synthase (DHPS) and the quorum-sensing regulator LasR. Their trajectories were compared to those of the corresponding apo proteins. Analyses included root-mean-square deviation (RMSD) for complex stability, root-mean-square fluctuation (RMSF) for residue-specific flexibility, radius of gyration (R_g) and solvent-accessible surface area (SASA) for global compactness, and principal component analysis (PCA) for essential collective motions. These detailed simulations provide a rigorous, time-evolved perspective on ligand-induced stabilization, directly supporting the static binding poses obtained from docking.

7.1 Stability and dynamics of DHPS complexes

The stability of the DHPS-ligand complexes was quantitatively assessed by monitoring the backbone RMSD relative to the initial minimized structure over the entire simulation trajectory (Fig. 12A and B). The RMSD for the **SMX033**-DHPS complex reached equilibrium rapidly, maintaining a low and stable profile with a mean value of 0.129 ± 0.020 nm. Similarly, the **SMX015**-DHPS complex exhibited a mean RMSD of 0.128 ± 0.030 nm. In contrast, the apo DHPS simulation displayed significantly higher and more variable instability, with a mean RMSD of 0.316 ± 0.070 nm. The substantially lower mean values and reduced standard deviations of the ligand-bound systems demonstrate that the binding of either **SMX033** or **SMX015** effectively constrains the protein backbone, inducing a more rigid and conformationally stable state compared to the apo protein. To elucidate localized effects, the per-residue flexibility was calculated *via* RMSF (Fig. 12C and D). The global backbone flexibility, expressed as the mean RMSF across all residues, was reduced in the presence of **SMX033** (0.105 ± 0.069 nm) and **SMX015** (0.111 ± 0.086 nm) relative to the apo protein (0.132 ± 0.107 nm). A critical observation was the pronounced dampening of fluctuations in key active site residues responsible for substrate binding and inhibitor interactions. For example, in the apo simulation, residues Phe^{28}, Arg^{63}, and Pro^{64} exhibited high fluctuations of 0.434 nm, 0.427 nm, and 0.556 nm, respectively. Upon binding **SMX033**, these fluctuations were reduced to 0.219 nm, 0.263 nm, and 0.366 nm. A comparable stabilizing trend was observed for the **SMX015** complex. Furthermore, residues involved in critical hydrogen-bonding networks with the sulfonamide core and substituents, such as Thr^{62}, Lys^{221}, and Ser^{222}, consistently demonstrated lower mobility in the bound states. This ligand-induced reduction in flexibility across the active site pocket indicates a stable occupation that restricts inherent dynamical motions, likely contributing to sustained enzyme inhibition.

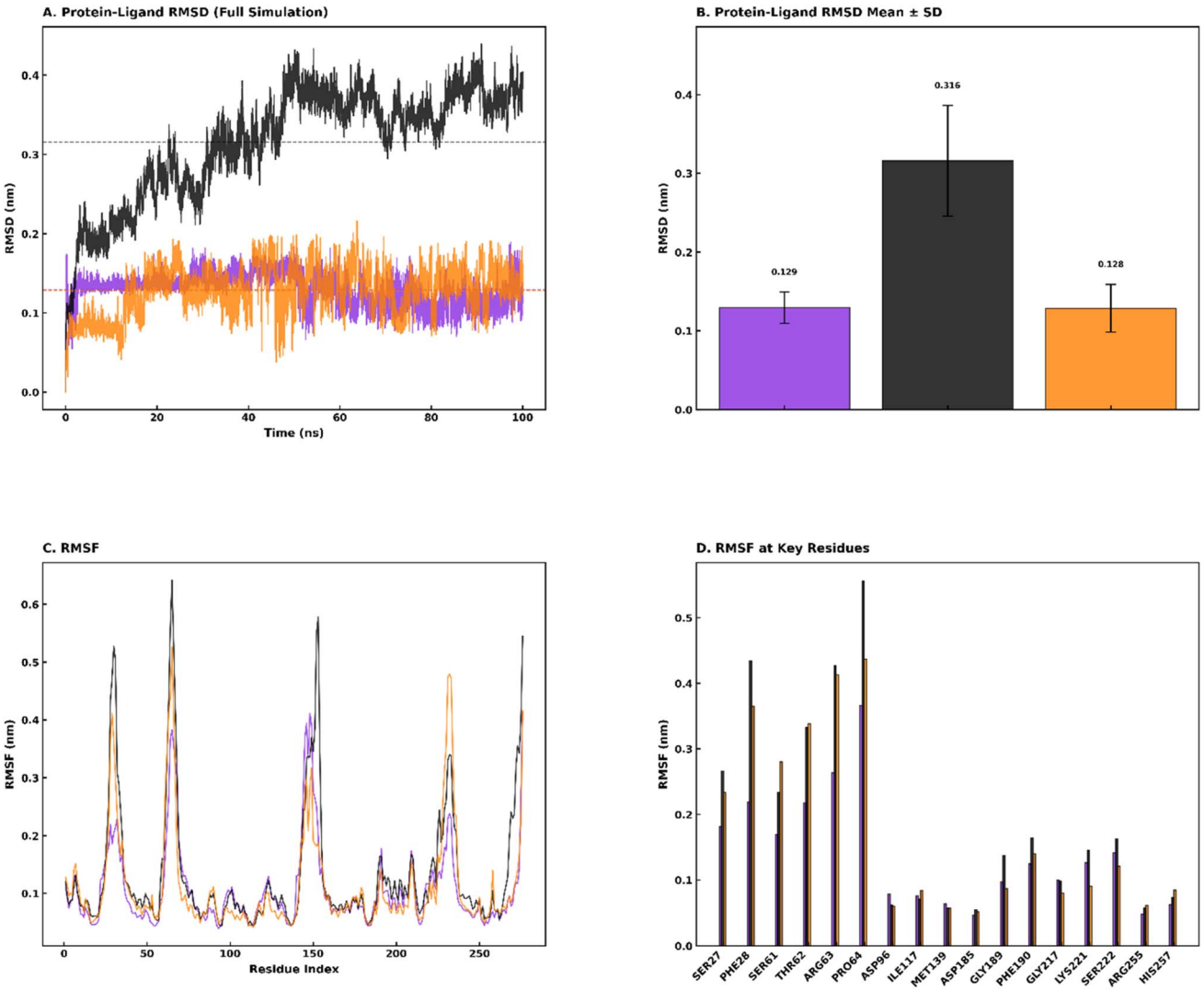

Fig. 12 Comparative analysis of the dynamic stability of DHPS in complex with **SMX015** (orange) and **SMX033** (purple), relative to apo DHPS (black). (A) Protein ligand RSMD; (B) protein lignad RSMD mean; (C) RMSF; (D) RSMF at key residues.

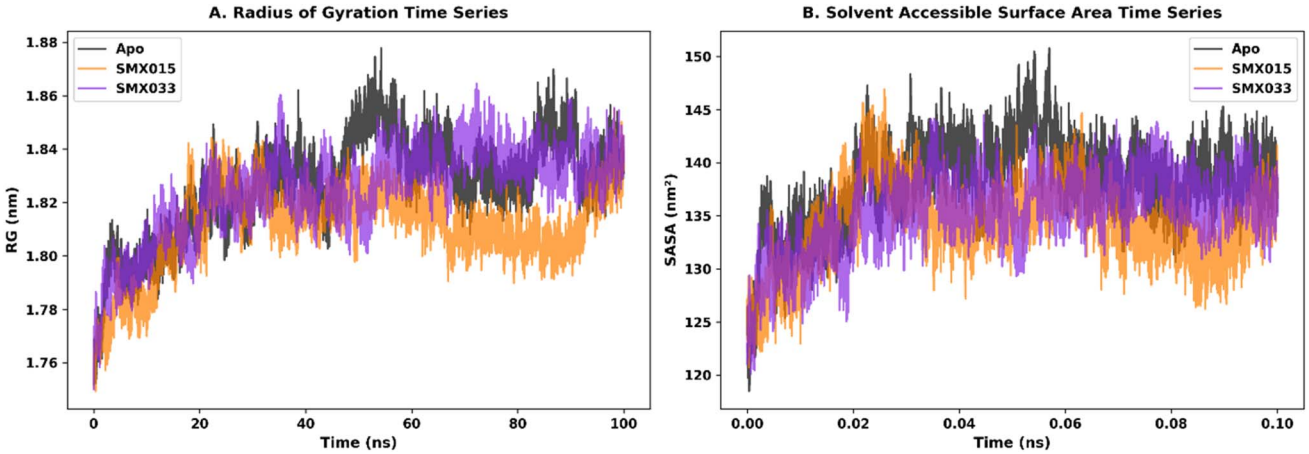

Fig. 13 Structural stability of apo DHPS (black) and DHPS in complex with SMX015 (orange) and SMX033 (purple), assessed by radius of gyration and solvent-accessible surface area. (A) Radius of gyration time series; (B) solvent accessible surface area time series.

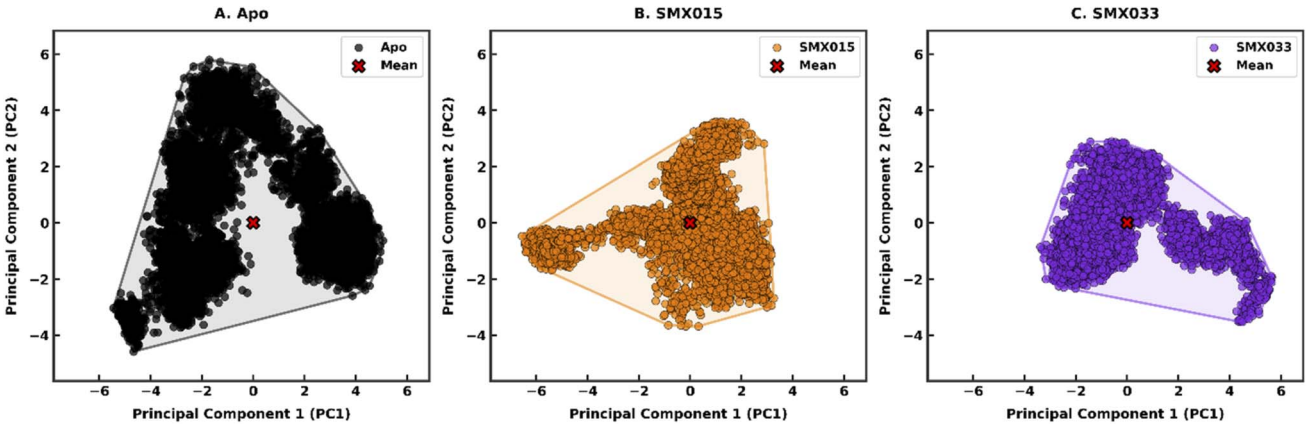

Fig. 14 SMX015-and SMX033-induced conformational landscapes of DHPS revealed by principal component analysis. (A) apo protein; (B) SMX015; (C) SMX033.

The global structural analysis of ligand binding were evaluated through the radius of gyration (R_g) and solvent-accessible surface area (SASA) (Fig. 13). The mean R_g for DHPS decreased from 1.827 ± 0.019 nm in the apo state to 1.811 ± 0.016 nm with **SMX015** and 1.824 ± 0.017 nm with **SMX033**. In addition, the mean SASA decreased from 138.2 ± 4.1 nm^2 (apo) to 134.2 ± 3.8 nm^2 (**SMX015**) and 135.4 ± 3.5 nm^2 (**SMX033**). The paired reduction in both R_g and SASA signifies a ligand-mediated contraction of the protein structure. This compaction is consistent with the stabilization of binding site loops and the burial of hydrophobic surfaces upon optimal ligand engagement, leading to a more globular and less solvent-exposed conformation.

To capture the large-scale, functionally relevant motions of DHPS, principal component analysis (PCA) was performed on the Cα atom trajectories (Fig. 14). The total variance captured by the first two principal components (PC1 and PC2) was substantially lower for the ligand-bound states: 7.36 ± 2.11 for **SMX015** and 5.18 ± 1.64 for **SMX033**, compared to 12.44 ± 3.87 for the apo protein. This marked reduction in collective motion variance indicates that binding of either derivative confines the protein's conformational sampling to a significantly more restricted subspace. The conformational space area, calculated from the projection of trajectories onto PC1 and PC2, was reduced by approximately 33% and 44% for the **SMX015** and **SMX033** complexes, respectively.

This analysis confirms that both ligands not only stabilize local binding site residues but also effectively dampen the global, low-frequency motions of the entire DHPS enzyme, effectively locking it into a stable conformation that is less prone to unproductive dynamics.

7.2 Stability and dynamics of LasR complexes

MD simulations of the LasR complexes revealed distinct dynamic profiles for the two ligands, correlating with their roles as quorum-sensing inhibitors. The backbone RMSD for the LasR-**SMX033** complex averaged 0.306 ± 0.062 nm, which was lower than both the apo protein (0.331 ± 0.095 nm) and the **SMX015** complex (0.338 ± 0.081 nm) (Fig. 15A and B). This suggests **SMX033** forms a marginally more stable complex

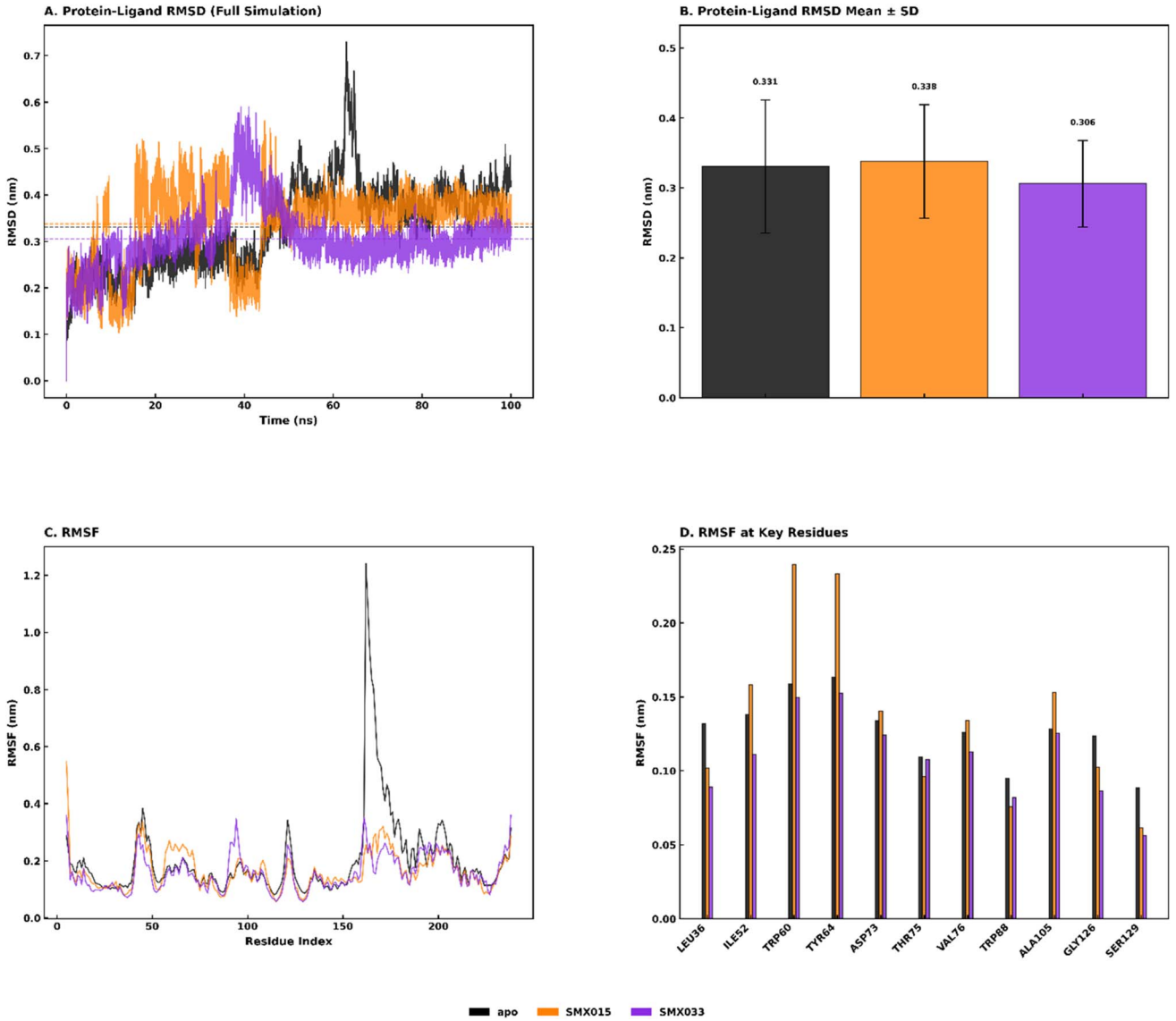

Fig. 15 Comparative analysis of the dynamic stability of LasR in complex with **SMX015** (orange) and **SMX033** (purple), relative to apo LasR (black). (A) Protein lignad RSMD; (B) protein ligand RSMD mean; (C) RMSF; (D) RMSF at key residues.

with LasR. RMSF analysis demonstrated that both ligands reduced the overall flexibility of LasR (mean RMSF: apo = 0.202 ± 0.149 nm; **SMX015** = 0.164 ± 0.067 nm; **SMX033** = 0.157 ± 0.062 nm). Notably, **SMX033** binding specifically reduced fluctuations in key hydrophobic cavity residues vital for autoinducer binding and protein dimerization (Fig. 15C and D). For instance, fluctuations of Leu^{36}, Ile^{52}, and Tyr^{64} were reduced to 0.089 nm, 0.111 nm, and 0.153 nm, respectively, from their higher apo values. While **SMX015** also exhibited a stabilizing effect, the magnitude of fluctuation reduction in these specific residues was less pronounced. This residue-specific stabilization supports the docking prediction that **SMX033** occupies and rigidifies the native ligand-binding site, potentially disrupting the conformational changes required for functional dimerization.

Analysis of the global parameters R_g and SASA indicated distinct ligand-dependent effects on the tertiary structure of LasR. The **SMX015** complex showed a slight decrease in mean R_g (1.912 ± 0.032 nm) and SASA (131.4 ± 3.0 nm^2) relative to apo-LasR (1.914 ± 0.036 nm; 133.0 ± 3.6 nm^2), indicating a mild compacting effect (Fig. 16). In contrast, the LasR-**SMX033** complex displayed a significant increase in both mean R_g (2.032 ± 0.025 nm) and SASA (137.4 ± 2.7 nm^2). This ligand-induced expansion suggests that **SMX033** binding triggers a distinct allosteric response, potentially causing structural rearrangements that propagate beyond the binding pocket. This expansion may be linked to the disruption of the dimerization interface, providing a dynamic rationale for its potent anti-biofilm activity *via* quorum-sensing inhibition.

PCA of the LasR trajectories further differentiated the ligands' effects. The total variance for the **SMX033**-bound

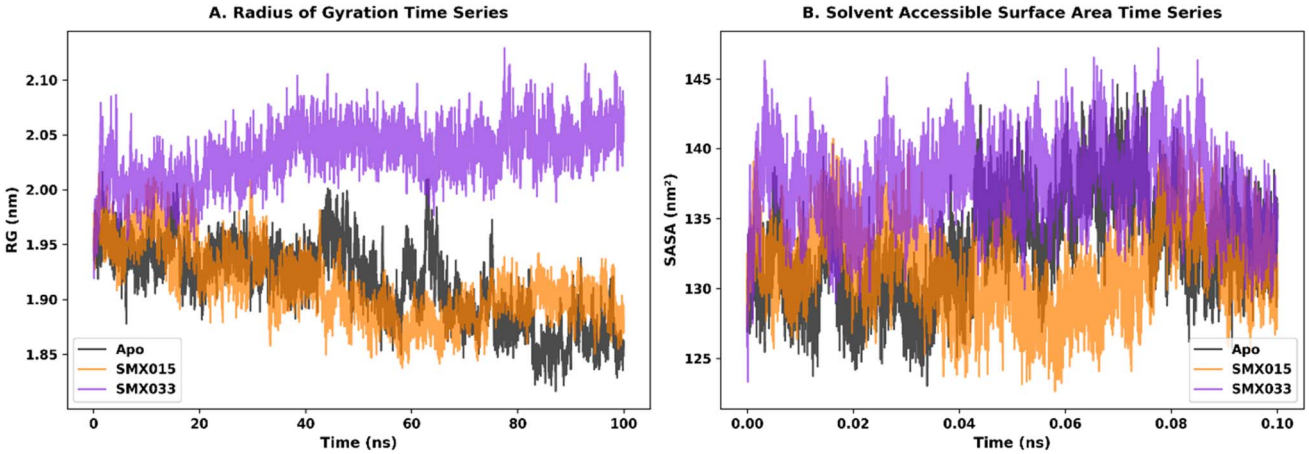

Fig. 16 Structural stability of apo LasR (black) and LasR in complex with SMX015 (orange) and SMX033 (purple), assessed by radius of gyration and solvent-accessible surface area. (A) Radius of gyration time series; (B) solvent accessible surface area time series.

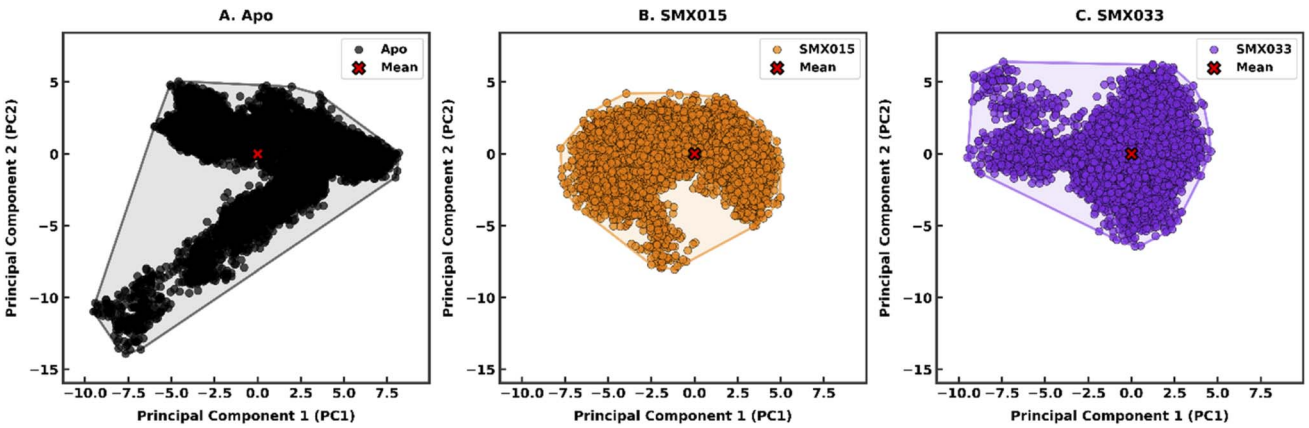

Fig. 17 SMX015- and SMX033-induced conformational landscapes of LasR revealed by principal component analysis. (A) Apo protein principal component 1; (B) SMX015 principal component; (C) SMX033 principal component.

system (8.38 ± 2.24) was dramatically lower than for the apo protein (24.07 ± 5.87) and the **SMX015**-bound system (11.39 ± 3.12) (Fig. 17). The profound reduction in collective motion for the **SMX033** complex indicates it imposes a more restriction on the intrinsic flexibility and essential dynamics of LasR. Although **SMX015** also reduced the conformational space area, its effect was less extensive. The capability of **SMX033** to significantly confine LasR's large-scale motions likely highlights its efficacy in biofilm inhibition, as it may more effectively prevent the conformational transitions necessary for LasR activation, DNA binding, and subsequent virulence gene expression.

The MD simulation analysis provide a robust, atomistic rationale for the experimentally observed biological efficacy of **SMX033** and **SMX015**. For DHPS, the pronounced stabilization of the active site architecture, suppression of key residue flexibility, and damping of global motions by both ligands correlate directly with their potent growth inhibitory activity (MIC = 15.625 μg mL^{-1}). This dynamic stabilization affirms their role as direct, high-affinity enzyme inhibitors. The superior biofilm inhibition (>99%) exhibited by both compounds, and particularly by **SMX033**, is dynamically supported by their stable binding and modulation of LasR. The unique dynamic signature of **SMX033** characterized by strong binding pocket stabilization, induction of an expanded protein state, and marked restriction of collective motions offers a compelling mechanism for its function as a quorum-sensing inhibitor. This aligns with the experimental observation of near-complete biofilm eradication. Consistent favorable dynamic behavior of **SMX033** across both targets supports its prioritization as the lead compound.

8 Conclusion

This study has successfully demonstrated a rational, integrated computational and experimental approach to design novel sulfamethoxazole derivatives that have potential to simultaneously target bacterial viability, virulence, and resistance mechanisms. Our structure-guided design yielded a focused library of derivatives, from which five candidates

were prioritized based on superior predicted binding affinities towards DHPS, the quorum-sensing regulator LasR, and the efflux pump transporter AcrB. The synthesis of these compounds was achieved efficiently, and their structures were unequivocally confirmed *via* NMR and HRMS. Biological evaluation revealed potent, broad-spectrum antimicrobial activity (MICs 15.625–125 μg mL^{-1}) against key ESKAPE pathogens, with lead compounds **SMX033** and **SMX015** exhibiting exceptional potency. Crucially, the experimental data strongly correlated with our *in silico* predictions. The derivatives achieved near-complete biofilm inhibition (>99%) by disrupting LasR-mediated quorum sensing, and **SMX033** emerged as a potent efflux pump inhibitor, directly corroborating our AcrB binding models. Furthermore, the markedly low cytotoxicity of **SMX033** ($CC_{50} = 286.20$ μM) underscores its promising selective toxicity and potential as a therapeutic scaffold. This work provides compelling proof-of-concept for a multi-targeting strategy to overcome multidrug resistance. By inhibiting DHPS, LasR, and AcrB concurrently, these sulfamethoxazole derivatives can attack the pathogen on multiple fronts, thereby mitigating the evolutionary pressure that leads to resistance. The excellent correlation between our computational predictions and experimental results establishes a validated blueprint for the potential rational design of next-generation antimicrobial agents. Future work will focus on *in vivo* efficacy studies, further medicinal chemistry optimization to improve potency and aqueous solubility and expanding this strategy to a broader chemical space to combat the ever-growing threat of pan-drug-resistant infections.

Author contributions

Cedric D. K. Amengor: supervised the project, developed the overall conceptual framework, oversaw the synthesis, wrote the original draft, and proofread the manuscript. Benedicta Yayra Adzah carried out the synthesis of the compounds. Prince Danan Biniyam: designed the computational conceptual framework and methodology, authored the molecular docking and MMGBSA, and proofread the manuscript. Ernest Oyeh, Vuvor Faustina and Yvonne Dogbeda Agboyibor assisted in the characterisation of the compounds. Victoria O. Adu: provided computational technical support for ADME analysis, assisted in data curation, and proofread the manuscript. Michael Osei: provided computational technical support for molecular docking, assisted in data curation, and proofread the manuscript. Kwabena Adu-Adjei: provided computational technical support for ADME analysis, assisted in data curation, and proofread the manuscript. Patrick Gyan, En Zhang, Ampomah-Wireko: contributed to the writing of the antitubercular section and proofread the manuscript. Paul Quansah and Cyril Makafui Amengor: provided mathematical and statistical support for antimicrobial data analysis. Joshua Boateng: interpreted the HRMS data and edited the first draft of the manuscript. Victoria Elmes: carried out the NMR analysis and provided technical expertise on the NMR instrumentation Iain Goodall: carried out the HRMS analysis and provided technical expertise on the mass spectrometer.

Conflicts of interest

The authors declare that they have no known competing financial interests or personal relationships that could have appeared to influence the work reported in this paper.

Data availability

The original contributions and data obtained in the study are presented in the article.

Supplementary information (SI): description of the spectroscopic data of the compounds. See DOI: https://doi.org/10.1039/d5ra08024j.

Acknowledgements

The authors would like to express their sincere gratitude to the technicians of the Synthetic Medicinal Chemistry and Computational Division at the School of Pharmacy, University of Health and Allied Sciences, for their invaluable support.

References

1 C. Xu, L. Kong, H. Gao, X. Cheng and X. Wang, *Front. Microbiol.*, 2022, **13**, 822689.
2 K. P. High, *Ageing Res. Rev.*, 2004, **3**, 1–14.
3 M. A. Salam, M. Y. Al-Amin, M. T. Salam, J. S. Pawar, N. Akhter, A. A. Rabaan and M. A. Alqumber, *Healthcare*, 2023, **11**, 1946.
4 A. P. Taylor, R. P. Robinson, Y. M. Fobian, D. C. Blakemore, L. H. Jones and O. Fadeyi, *Org. Biomol. Chem.*, 2016, **14**, 6611–6637.
5 J. Jampilek, *Molecules*, 2019, **24**, 3839.
6 G. Shabir, A. Saeed, W. Zahid, F. Naseer, Z. Riaz, N. Khalil and F. Albericio, *Pharmaceuticals*, 2023, **16**, 1162.
7 S. Kumari, A. V. Carmona, A. K. Tiwari and P. C. Trippier, *J. Med. Chem.*, 2020, **63**, 12290–12358.
8 G. J. Martis and S. L. Gaonkar, *RSC Adv.*, 2025, **15**, 8213–8243.
9 S. Li, Y. Mei, L. Jiang, X. Yang, W. Zeng and Y. Du, *RSC Med. Chem.*, 2025, DOI: 10.1039/D4MD00777H.
10 S. Ramlakhan, V. Singh, J. Stone and A. Ramtahal, *Clin. Med. Insights Pediatr.*, 2014, **8**, CMPed–S8100.
11 H. Sørum, in *Antimicrobial Resistance in Bacteria of Animal Origin*, ed. F. M. Aarestrup, ASM Press, 2005, pp. 213–238.
12 B. Jubeh, Z. Breijyeh and R. Karaman, *Molecules*, 2020, **25**, 2888.
13 M. Pervaiz, A. Riaz, A. Munir, Z. Saeed, S. Hussain, A. Rashid and A. Adnan, *J. Mol. Struct.*, 2020, **1202**, 127284.
14 M. Claudel, J. V. Schwarte and K. M. Fromm, *Chemistry*, 2020, **2**, 849–899.
15 S. Wang, H. Y. Zhang, L. Wang, Z. J. Duan and I. Kennedy, *Food Addit. Contam.*, 2006, **23**, 362–384.
16 S. Ballav, D. Jana, K. C. Guchhait, B. Das, M. Manna, S. Hazra and C. Ghosh, in *Biofilm Associated Antimicrobial Resistance and its Recovery*, CRC Press, 2023, pp. 66–81.
17 R. Alenazy, *J. King Saud Univ. Sci.*, 2022, **34**, 102275.

18 V. C. Scoffone, G. Trespidi, G. Barbieri, S. Irudal, E. Perrin and S. Buroni, *Antibiotics*, 2021, **10**, 863.
19 L. M. A. Ghany, N. Ryad, M. S. Abdel-Aziz, H. M. Abd El-Lateef, I. Zaki and B. Y. Beshay, *J. Mol. Struct.*, 2024, **1309**, 138170.
20 F. Giordanetto, P. W. Fowler, M. Saqi and P. V. Coveney, *Philos. Trans. R. Soc. London, A*, 2005, **363**, 2055–2073.
21 C. A. Salubi, *Molecular Docking Investigation and Pharmacokinetic Properties Prediction of Some Benzimidazole Analogues as Dihydropteroate Synthase (DHPS) Inhibitors*, 2023.
22 Z. Breijyeh and R. Karaman, *Antibiotics*, 2023, **12**, 628.
23 T. Hanai, *Front. Med. Chem.*, 2009, **4**, 86–129.
24 H. Azevedo-Barbosa, B. P. do Vale, G. Guidolin Rossi, F. dos Santos Siqueira, K. Bordignon Guterres, M. M. A. de Campos and D. Teixeira Carvalho, *Chem. Biodiversity*, 2021, **18**, e2100066.
25 D. Das, N. Sahu, S. Roy, P. Dutta, S. Mondal, E. L. Torres and C. Sinha, *Spectrochim. Acta, Part A*, 2015, **137**, 560–568.
26 J. P. Fetse, J. O. Kyekyeku, E. Dueve and K. B. Mensah, *Br. J. Pharm. Res.*, 2014, **4**, 2642.
27 C. Agyare, A. S. Dwobeng, N. Agyepong, Y. D. Boakye, K. B. Mensah, P. G. Ayande and M. Adarkwa-Yiadom, *Adv. Pharmacol. Pharm. Sci.*, 2013, **2013**, 692613.
28 M. Ofori, C. A. Danquah, S. Ativui, P. Doe and W. A. Asamoah, *Biomed. Pharmacol. J.*, 2021, **14**(4), 1905–1915.
29 C. A. Danquah, P. A. B. Minkah, T. A. Agana, P. Moyo, M. Tetteh, I. O. D. Junior and V. J. Maharaj, *et al.*, Natural Products as Antibiofilm Agents, *Focus on bacterial biofilms*, 2022, p. 203.
30 D. Anokwah, E. Asante-Kwatia, J. Asante, D. Obeng-Mensah, C. A. Danquah, I. K. Amponsah and A. Y. Mensah, *Microorganisms*, 2023, **12**, 7.
31 R. Mowla, Y. Wang, S. Ma and H. Venter, *Biochim. Biophys. Acta, Biomembr.*, 2018, **1860**, 878–886.
32 K. Azeem, S. Fatima, A. Ali, A. Ubaid, F. M. Husain and M. Abid, *Life*, 2025, **15**, 49.
33 X. He, S. Liu, T. S. Lee, B. Ji, V. H. Man, D. M. York and J. Wang, *ACS Omega*, 2020, **5**, 4611–4619.
34 P. Bhadra and S. W. Siu, *Langmuir*, 2019, **35**, 9622–9633.
35 H. Grabski, L. Hunanyan, S. Tiratsuyan and H. Vardapetyan, *F1000Research*, 2019, **8**, 324.
36 N. Singh and A. Warshel, *Proteins: Struct., Funct., Bioinf.*, 2010, **78**, 1705–1723.
37 D. Van Der Spoel, E. Lindahl, B. Hess, G. Groenhof, A. E. Mark and H. J. Berendsen, *J. Comput. Chem.*, 2005, **26**, 1701–1718.
38 S. Jo, X. Cheng, J. Lee, S. Kim, S. J. Park, D. S. Patel and W. Im, *J. Comput. Chem.*, 2017, **38**, 1114–1124.
39 R. Shukla and T. Tripathi, in *Computer-aided Drug Design*, Springer, Singapore, 2020, pp. 133–161.
40 K. Vanommeslaeghe, E. Hatcher, C. Acharya, S. Kundu, S. Zhong, J. Shim and A. D. Mackerell Jr, *J. Comput. Chem.*, 2010, **31**, 671–690.
41 G. J. Martis and S. L. Gaonkar, *RSC Adv.*, 2025, **15**, 8213–8243.
42 M. A. Subbaiah and N. A. Meanwell, *J. Med. Chem.*, 2021, **64**, 14046–14128.
43 E. Marsault and M. L. Peterson, *J. Med. Chem.*, 2011, **54**, 1961–2004.
44 K. J. Coe, *PhD Thesis*, University of Washington, 2008.
45 C. Saran and K. L. Brouwer, *Toxicol. Pathol.*, 2023, **51**, 405–413.
46 Z. Wang, H. Sun, X. Yao, D. Li, L. Xu, Y. Li and T. Hou, *Phys. Chem. Chem. Phys.*, 2016, **18**, 12964–12975.
47 R. Jakhar, M. Dangi, A. Khichi and A. K. Chhillar, *Curr. Bioinf.*, 2020, **15**, 270–278.
48 A. H. Bakheit, M. W. Attwa, A. A. Kadi, H. A. Ghabbour and H. M. Alkahtani, *Crystals*, 2023, **13**, 1020.
49 J. W. M. Nissink and S. Degorce, *Future Med. Chem.*, 2013, **5**, 753–767.
50 C. A. Salubi, *Molecular Docking Investigation and Pharmacokinetic Properties Prediction of Some Benzimidazole Analogues as Dihydropteroate Synthase (DHPS) Inhibitors*, 2023.
51 C. R. Bourne, *Antibiotics*, 2014, **3**, 1–28.
52 M. N. Nalam, A. Ali, M. D. Altman, G. S. Reddy, S. Chellappan, V. Kairys, A. Ozen, H. Cao, M. K. Gilson, B. Tidor, T. M. Rana and C. A. Schiffer, *J. Virol.*, 2010, **84**, 5368–5378.
53 K. A. Ayers, *PhD Thesis*, The University of Tennessee Health Science Center, 2009.
54 S. Genheden and U. Ryde, *Expert Opin. Drug Discovery*, 2015, **10**, 449–461.
55 M. Zürcher and F. Diederich, *J. Org. Chem.*, 2008, **73**, 4345–4361.
56 H. X. Zhou and X. Pang, *Chem. Rev.*, 2018, **118**, 1691–1741.
57 M. Shah, V. L. Taylor, D. Bona, Y. Tsao, S. Y. Stanley, S. M. Pimentel-Elardo and K. L. Maxwell, *Mol. Cell*, 2021, **81**, 571–583.
58 P. Di Fruscia, A. Carbone, G. Bottegoni, F. Berti, F. Giacomina, S. Ponzano and F. Bertozzi, *J. Med. Chem.*, 2021, **64**, 13327–13355.
59 D. Drew, M. M. Klepsch, S. Newstead, R. Flaig, J. W. De Gier, S. Iwata and K. Beis, *Mol. Membr. Biol.*, 2008, **25**, 677–682.
60 L. Bibens, J. P. Becker, A. Dassonville-Klimpt and P. Sonnet, *Pharmaceuticals*, 2023, **16**, 425.
61 J. Mehla, G. Malloci, R. Mansbach, C. A. López, R. Tsivkovski, K. Haynes and H. I. Zgurskaya, *mBio*, 2021, **12**, 10–1128.
62 M. Baym, L. K. Stone and R. Kishony, *Science*, 2016, **351**, aad3292.
63 H. C. Flemming and J. Wingender, *Nat. Rev. Microbiol.*, 2010, **8**, 623–633.
64 N. Rabin, Y. Zheng, C. Opoku-Temeng, Y. Du, E. Bonsu and H. O. Sintim, *Future Med. Chem.*, 2015, **7**, 493–512.
65 S. Singh, S. Datta, K. B. Narayanan and K. N. Rajnish, *J. Genet. Eng. Biotechnol.*, 2021, **19**, 140.
66 R. Elawady, A. G. Aboulela, A. Gaballah, A. A. Ghazal and A. N. Amer, *BMC Infect. Dis.*, 2024, **24**, 1065.
67 X. Wang, M. Liu, C. Yu, J. Li and X. Zhou, *Mol. Biomed.*, 2023, **4**, 49.
68 M. E. Skogman, P. M. Vuorela and A. Fallarero, *J. Antibiot.*, 2012, **65**, 453–459.

69 A. Gaurav, P. Bakht, M. Saini, S. Pandey and R. Pathania, *Microbiology*, 2023, **169**, 001333.
70 M. AlMatar, O. Albarri, E. A. Makky and F. Köksal, *Pharmacol. Rep.*, 2021, **73**, 1–16.
71 L. Huang, C. Wu, H. Gao, C. Xu, M. Dai, L. Huang and G. Cheng, *Antibiotics*, 2022, **11**, 520.
72 A. Lamut, L. Peterlin Mašič, D. Kikelj and T. Tomašič, *Med. Res. Rev.*, 2019, **39**, 2460–2504.
73 L. Zhang, X. Tian, L. Sun, K. Mi, R. Wang, F. Gong and L. Huang, *Pharmaceutics*, 2024, **16**, 170.
74 S. Nafisi, A. A. Saboury, N. Keramat, J. F. Neault and H. A. Tajmir-Riahi, *J. Mol. Struct.*, 2007, **827**, 35–43.
75 S. Pal, A. Misra, S. Banerjee and B. Dam, *J. King Saud Univ. Sci.*, 2020, **32**, 939–945.
76 P. W. Limaverde, F. F. Campina, F. A. da Cunha, F. D. Crispim, F. G. Figueredo, L. F. Lima and S. R. Tintino, *Food Chem. Toxicol.*, 2017, **109**, 957–961.
77 S. R. Tintino, C. D. Oliveira-Tintino, F. F. Campina, P. Weslley Limaverde, P. S. Pereira, J. P. Siqueira-Junior and V. Q. Balbino, *Med. Chem. Res.*, 2018, **27**, 261–267.
78 J. Olmsted III and D. R. Kearns, *Biochemistry*, 1977, **16**, 3647–3654.
79 D. Olender, J. Żwawiak and L. Zaprutko, *Pharmaceuticals*, 2018, **11**, 54.